

# **Contents**

<b>List of figures</b>	<b>v</b>
<b>List of tables</b>	<b>vi</b>
<b>1 Introduction</b>	<b>1</b>
<b>2 Theoretical background</b>	<b>2</b>
2.1 Closed and open cylindrical pores . . . . .	2
2.2 Kelvin equation . . . . .	2
2.3 Condensation and evaporation in non ideal pores . . . . .	4
2.3.1 Condensation and evaporation in a closed straight pore . . . . .	4
2.3.2 Condensation and evaporation in a closed funnelled pore . . . . .	4
2.3.3 Condensation and evaporation in an open straight pore . . . . .	8
2.3.4 Condensation and evaporation in an open funnelled pore . . . . .	8
2.4 Transmission of a nanoporous alumina membrane . . . . .	8
2.4.1 Effective medium approximation . . . . .	8
2.4.2 Fresnel transmission coefficient of nanoporous alumina membranes . . . . .	9
2.5 Light scattering in alumina membranes . . . . .	9
<b>3 Experimental</b>	<b>11</b>
3.1 Membrane production . . . . .	11
3.1.1 Anodizing . . . . .	11
3.1.2 Aluminum dissolution . . . . .	13
3.1.3 Barrier layer dissolution . . . . .	14
3.1.4 Atomic layer deposition . . . . .	14
3.1.5 Terminology . . . . .	16
3.2 Scanning electron microscopy . . . . .	16
3.2.1 Statistical evaluation of the SEM images . . . . .	17
3.3 Experimental setup . . . . .	17
3.3.1 Volumetric setup . . . . .	17
3.3.1.1 Cell temperature regulation . . . . .	19
3.3.1.2 Pressure gauges . . . . .	19
3.3.2 Laser transmission setup . . . . .	19
3.3.3 Camera setup . . . . .	19
3.4 Experimental procedure . . . . .	19
3.4.1 Bypass . . . . .	20
3.4.1.1 Changing the membrane . . . . .	21
3.5 Isotherm computation . . . . .	21
3.5.1 Volumetric isotherm . . . . .	21
3.5.1.1 Porosity . . . . .	23
3.5.1.2 Determination of the saturated vapor pressure . . . . .	24
3.5.1.3 Diameter error using Kelvin equation . . . . .	24
3.5.2 Optical measurements . . . . .	24

<b>4 Experimental results</b>	<b>26</b>
4.1 Experimental approach . . . . .	26
4.2 Membrane structure analysis . . . . .	26
4.2.1 Isotherm of an open pore membrane . . . . .	26
4.2.2 Isotherm of a closed pore membrane . . . . .	28
4.2.3 Measurement reproducibility . . . . .	29
4.2.4 Inhomogeneities on one wafer . . . . .	31
4.2.4.1 Transmission of open and closed pores . . . . .	32
4.2.5 Defects . . . . .	32
4.3 The problem of pore opening . . . . .	36
4.3.1 Bad open pores . . . . .	36
4.3.2 Etch rate on the barrier layer . . . . .	38
4.3.3 Increase of funnellization upon immersion in phosphoric acid . . . . .	39
4.3.4 Inverse funnellization upon barrier layer dissolution . . . . .	42
<b>Bibliography</b>	<b>45</b>

## List of Figures

2.1	Menisci of the condensation and evaporation processes within a closed pore (a) and an open pore (b). For a closed pore, condensation and evaporation both occur at equilibrium pressure yielding spherical menisci. In contrast, the condensation in an open pore occurs at spinodal pressure with a cylindrical meniscus. The evaporation remains behaves unchanged occurring at equilibrium pressure. . . . .	3
2.2	Pressure to diameter conversion by KELVIN equation for the parameters $T = 19^\circ\text{C}$ , $\gamma_{T=19^\circ\text{C}}^{\text{hexane}} = 0,018\,605 \frac{\text{N}}{\text{m}}$ and $V_{\text{mol}, T=19^\circ\text{C}}^{\text{hexane}} = 0,130\,53 \frac{\text{L}}{\text{mol}}$ . . . . .	3
2.3	Condensation and evaporation isotherm model of a closed cylindrical pore. (a) corresponds to the mechanisms in a straight pore whereas (b) does for a funnelled one. The corresponding processes inside the pore are illustrated below the isotherm itself. Colors of the arrows between pore states and the respecting pressure range of the graph match. . . . .	5
2.4	Condensation (a) and evaporation (b) isotherm of an open straight pore. The corresponding processes inside the pore are illustrated below the isotherm itself. Colors of the arrows between pore states and the respecting pressure range of the graph match. . . . .	6
2.5	Condensation (a) and evaporation (b) isotherm of an open funnelled pore. The corresponding processes inside the pore are illustrated below the isotherm itself. Colors of the arrows between pore states and the respecting pressure range of the graph match. . . . .	7
2.6	Absorption and desorption isotherm loops for closed pores (a) and open pores (b). For the funnelled pores it is $d > d'$ . . . . .	9
2.7	Illustration of the idea behind the effective medium approximation applied on the refractive index of a porous medium (compare section 2.4.1). . . . .	10
3.1	Setup for the anodizing of the membrane production. The aluminum wafer functions as anode while a platinum plate makes for the cathode. The oxalic acid is stirred during the whole process. . . . .	12
3.2	Production stages of the membrane production. It starts with a wafer of bulk aluminum (dark gray) (a) which is then anodized yielding (b), where light gray represents alumina. The latter is then dissolved producing a bulk aluminum wafer with hexagonally arranged hollows (c). By the second anodizing, straight parallel pores are created (d). After dissolving the remaining aluminum (e), the barrier layer etched to open the pores (f). The initial aluminum wafer's thickness is $d_{\text{Al}} = 1 \text{ mm}$ , the <i>barrier layer</i> thickness $d_{\text{barrier-layer}}$ is 30 nm to 60 nm, the pore diameters $d_{\text{pore}} = 10 \text{ nm}$ to 100 nm and the pore length or membrane thickness $l_{\text{pore}} = 30 \mu\text{m}$ to 60 $\mu\text{m}$ . . . . .	13
3.3	(a) shows the setup for the aluminum dissolution step. The wafer is immersed in acid composed according to eq. (3.1) which dissolves aluminum. In (b) the <i>barrier layer</i> dissolution by floating the membrane on phosphoric acid is illustrated. . . . .	14
3.4	Photos taken during the <i>barrier layer</i> dissolution step. (a) shows the milky aspects that appear during the floating of the wafers. In (b), a film of phosphoric acid covers the whole wafer at the end of the process. . . . .	15
3.5	Illustration of the atomic layer deposition process. For explanations please refer to section 3.1.4. . . . .	16

3.6	Vapor pressure of hexane according to ANTOINE equation (eq. (3.5)) using the ANTOINE equation parameter eq. (3.6) for hexane. . . . .	18
3.7	Experiment setup. The temperatures within the reservoir and the cell are measured by the thermometers $T_{\text{res}}$ and $T_{\text{cell}}$ . Furthermore, $P_{\text{res}}$ and $P_{\text{cell}}$ are the two installed pressure gauges. The void is experimentally realized by a primary pump. . . . .	18
3.8	Sketch of the laser transmission setup. . . . .	19
3.9	Final experiment setup. With respect to fig. 3.7, the bypass allows to pump the whole system without changing the opening of the PFEIFFER microvalve. Furthermore, the laser transmission setup and the camera setup are outlined. . . . .	20
3.10	Raw volumetric isotherm data recorded with the experimental setup as explained in section 3.4 for one cycle without a membrane inside the cell and one with a membrane inside the cell. (a) shows the pressure values over time making the condensation and evaporation plateaus of absorption and desorption of hexane within the membrane's pores visible. (b) is the pressure loop which is relevant for the computation of the isotherms. Again, the before mentioned plateaus are visible as dips in the time derivative of the pressure. . . . .	22
3.11	(a) shows the raw data of the isotherm with membrane and interpolation of the reference isotherm without membrane. Also, the subtraction of the latter (compare integrand of eq. (3.11)) is plotted where the area to be integrated for the absorption and desorption isotherm is shaded light green. The integration according to eq. (3.12) results in the isotherm displayed in (b). . . . .	23
4.1	Convention used to assign membrane depending on their position on the wafer. . . . .	26
4.2	Wafer 295 and 296 processing scheme. While a  signifies a recorded isotherm, the  means MEB pictures have been taken. Red marks pores closed on one end, green pores open on both ends. The processed wafers are immersed in phosphoric acid for $t_{\text{immerse}}$ or floated on for $t_{\text{float}}$ . . . . .	27
4.3	Measurement results of open pore membrane 296b'. The dashed lines mark the average condensation and evaporation pressures. . . . .	29
4.4	SEM images of membrane 295g' implying the pores' funnellization. The pores on the solution side (a) show bigger diameters than those on the aluminum side (b). . . . .	30
4.5	Measurement results of closed pore membrane 296b in comparison to the open pore membrane 296b'. . . . .	31
4.6	Reproducibility test comparing multiple isotherms measured for the same membrane 292c. . . . .	32
4.7	Comparison of closed pore membranes of one wafer. (a) compares membranes of wafer 296 while fig. 4.7(b) deals with 295. . . . .	33
4.8	Comparison of open pore membranes of one wafer. (a) compares membranes of wafer 292 while fig. 4.8(b) deals with 295. . . . .	34
4.9	Transmission measurements of wafer 296 (a) and wafer 295 (b). Wafer 296 has been measured in untreated closed pore state. The membranes 295a and 295b are closed pore membranes while the rest of wafer 295 has been opened. . . . .	35
4.10	Bad open pores illustrated by the comparison of a closed pore isotherm and a open pore isotherm of membrane 294a. . . . .	36
4.11	(a) shows a SEM image confirming the bad open pores of membrane 294op. Image (b) SEM image of a membran floated on phosphoric acid until the appearance of milky aspects. It is coherent with the link of the milky aspect to pores of a wafer starting to open. . . . .	37
4.12	Confirmation that the membranes 296c', 296d', 296e' and 296f' are still closed pore membranes after the treatments with phoysphoric acid. The shapes of their isotherms match those of the untreated closed pore membranes 296a and 296b, wheras they do not show any shift of the condensation branch in direction of that of open pore membrane 296b'. . . . .	39

4.13 SEM images with the aim to measure the thickness of the <i>barrier layer</i> of the membranes 296c' and 296e' . . . . .	40
4.14 Membrane 296c' has been immersed in phosphoric acid for $t_{296c'} = 13$ min, 296d' for $t_{296d'} = 26$ min. (a) shows the isotherms of the immersion experiment conducted using wafer 296. The shift to larger pressures of the beginning of the evaporation branch and the unmoving beginning of the condensation branch are clearly visible. (b) and (c) are higher resolution plots of the relevant areas of the evaporation and respectively condensation branch of the isotherm on a pore diameter scale. . . . .	41
4.15 Immersion of a closed pore membrane resulting in an increase of the funnelling aspect of the pores as shown in (b) due to the saturation of the acid within the pores. The visualized theory is backed by the isotherms in fig. 4.14(a) which lead to the etch rate dependency plotted in (a) on the height within a pore. For further explanations please refer to section 4.3.3. . . . .	42
4.16 Comparison of the isotherms of membranes with closed pores to those with open pores. (a) shows membranes of wafer 296, while (b) displays those of wafer 295. The increase of size of the hysteresis is clearly observable. . . . .	43
4.17 Possible shape interpretation of the volumetric isotherms of membrane 295a for a single pore. If the interpretation were correct, an incontinuity ?? of the anodizing current could be the reason for the change in funnelling. . . . .	44

## List of Tables

4.1	Wafer specifications. The wafers thickness $l_{\text{pore}}$ , floating time $t_{\text{float}}$ of the <i>barrier layer</i> dissolution process and pore diameter dispersion $\Delta d_{\text{pore}}^{\text{MEB}}$ measured by electron beam microscopy are noted. The latter two parameters apply to the open pore membranes of the respective wafer. . . . .	28
4.2	Diameter reduction per minute of immersion derived from the isotherms of the membranes 296a, 296c, 296d. . . . .	42

# 1 Introduction

The team I conducted my internship in studies condensation and evaporation of helium in different confined materials. During the last 18 months the group focused on nanoporous membranes as a model system of pores of well defined diameters. The goal of these experiments is to measure the dependency of the pressure, at which the condensation and evaporation occur within the pores, on the pore diameters and the temperature relative to the critical temperature and to compare the results to theoretical models. In this respect, the advantage of helium is the ease of changing the temperature in a large range in respect to the critical temperature  $T_c$  from  $\frac{T_c}{4}$  to  $T_c$  in the setup.

Nanoporous alumina membranes are widely used for ??? (ref). Typically they have a thickness of several tens of micrometers with pores aligned orthogonally to the membrane's surface. At *Institut Néel*, they are synthesized by Laurent Cagnon using an anodization process. The typical pore diameters ranges from 40 nm to 60 nm with an inter pore distance of 100 nm to 120 nm. Smaller diameters are then obtained by using atomic layer deposition (ALD) of alumina.

At *Institut Néel*, the observation of condensation and evaporation makes use of macroscopic techniques which are volumetric isotherm and light scattering measurements. Hereby, the pressure at which condensation and evaporation occurs is averaged over a very large number of pores. Determining the pore diameters from these quantities therefore requires the production of membranes that are as monodisperse as possible.

The used membranes are characterized by two methods. First, absorption and desorption experiments using hexane as a fluid are conducted. The advantage of hexane over helium is that it allows experimenting at room temperature which makes for much faster executable experimentation. Second, reflection electron microscopy (REM) of the pore ends and the membranes' cross sections.

When the author of this text arrived at *Institut Néel* at the beginning of his internship, experiments with several membranes had already revealed that condensation and evaporation occurred over a relatively broad range of pressures revealing a dispersion of pore diameters. This dispersion could be attributed to multiple effects which are the diameter variation along the length of a single pore (due to funnellization and/ or corrugations) and the distribution of the pores' diameters.

The goals of the internship were then the following:

- Improving and systemizing the evaluation of the recorded isotherm data
- Performing isotherm measurements on many membranes as to confirm the previously reached conclusions statistically
- Comparing the pore diameters extracted from the volumetric measurements to the ones extracted from the REM results
- Improving the fabrication process to reduce the dispersion
- Testing the efficiency of the ALD process as a means to reduce the pore diameters.

Outlines to come..

In the following,

## 2 Theoretical background

### 2.1 Closed and open cylindrical pores

For simplification, in the following, the term *closed pore* will refer to a cylindrical pore that is closed on one end, whereas an *open pore* is open on both ends. Due to production processes, closed funnelled pores are always closed on the small end leaving the end with the larger diameter open.

### 2.2 Kelvin equation

Condensation of a fluid in a cylindrical pore occurs at pressures below the saturated vapor pressure  $P_{sv}$ . For relatively large pores, this is dominantly due to the fluid's surface tension. For a curved meniscus, LAPLACE-YOUNG equation implies

$$P_l - P_v = -\gamma \underbrace{\left( \frac{1}{R_1} + \frac{1}{R_2} \right)}_{:=\zeta}$$

with the pressure inside the liquid  $P_l$ , pressure inside the vapor  $P_v$ , surface tension  $\gamma$  and meniscus radii  $R_1$ ,  $R_2$  and  $\zeta$  the meniscus mean curvature. Connecting this with the phase equilibrium

$$\mu_l(P_l) = \mu_v(P_v),$$

where  $\mu_l$  is the chemical potential within the liquid,  $\mu_v$  the one within the vapor, determines the vapor and the liquid pressure. For an incompressible liquid and a perfect vapor, the phase equilibrium becomes

$$\begin{aligned} \mu_l(P_l) &= \mu_l(P_{sv}) + V_{mol}^l(P_l - P_{sv}), \\ \mu_v(P_v) &= \mu_v(P_{sv}) + RT \ln \underbrace{\left( \frac{P_v}{P_{sv}} \right)}_{:=P_{rel}}, \end{aligned}$$

with the molar volume of the liquid  $V_{mol}^l$ , the ideal gas constant  $R$  and the temperature of the system  $T$ . Using the definition

$$\mu_v(P_{sv}) = \mu_l(P_{sv})$$

and assuming the liquid to be much denser than the, yields

$$-\zeta V_{mol}^l = RT \ln P_{rel}, \quad (2.1)$$

the so called KELVIN equation.  $P_{rel}$  shall be referred to as the relative vapor pressure from here on.

For a perfectly wetting liquid the meniscus in a closed pore, the meniscus curvature is

$$\zeta_{sph} = \frac{1}{R_0} + \frac{1}{R_0} = \frac{2}{R_0}$$

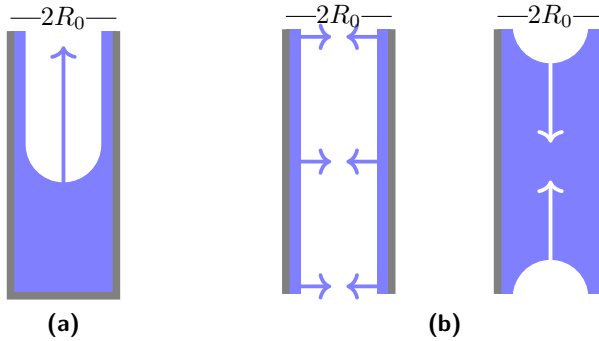


**Figure 2.1** Menisci of the condensation and evaporation processes within a closed pore (a) and an open pore (b). For a closed pore, condensation and evaporation both occur at equilibrium pressure yielding spherical menisci. In contrast, the condensation in an open pore occurs at spinodal pressure with a cylindrical meniscus. The evaporation remains unchanged occurring at equilibrium pressure.

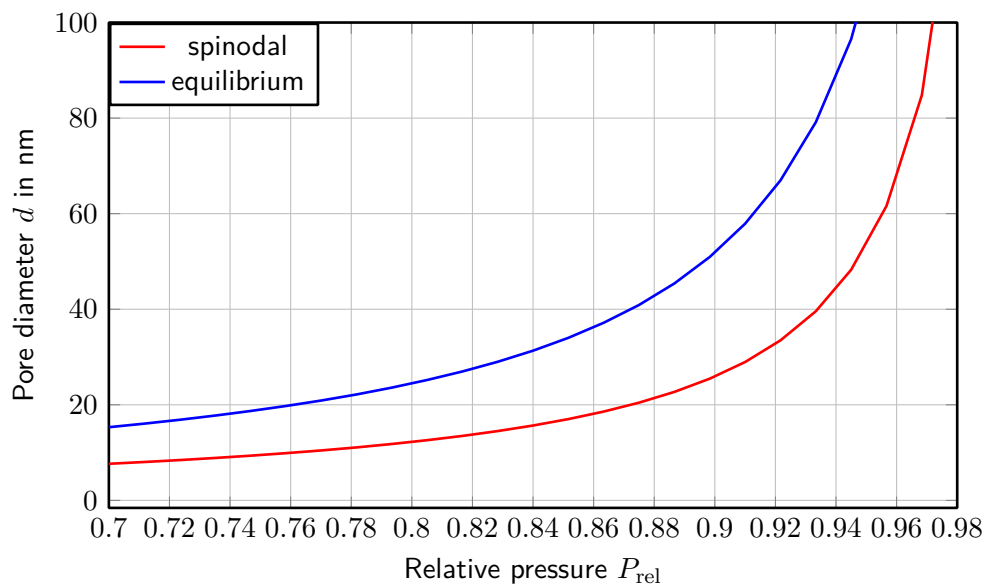


**Figure 2.2** Pressure to diameter conversion by KELVIN equation for the parameters  $T = 19^\circ\text{C}$ ,  $\gamma_{T=19^\circ\text{C}}^{\text{hexane}} = 0,018\,605 \frac{\text{N}}{\text{m}}$  and  $V_{\text{mol}, T=19^\circ\text{C}}^{\text{hexane}} = 0,130\,53 \frac{\text{L}}{\text{mol}}$ .

with the pore diameter  $R_0$ . The result is a shift of the condensation pressure  $P_{\text{cond}}$  from  $P_{\text{sv}}$  to equilibrium pressure

$$P_{\text{eq}} = P_{\text{sv}} \cdot \exp\left(-\frac{2 \cdot \gamma V_{\text{mol}}^1}{R_0 \cdot RT}\right) < P_{\text{sv}}. \quad (2.2)$$

Figure 2.1(a) shows the reversibility of the process resulting in the evaporation pressure being

$$P_{\text{evap}} = P_{\text{cond}}.$$

Regarding an open pore - again assuming a perfectly wetting liquid - a hysteresis appears. Unlike for the closed pore, the liquid cannot nucleate from the bottom in this case. In the absence of thermally activated nucleation of a liquid bridge, condensation only occurs due to the collapse of the cylindrical liquid film absorbed on the walls. If the film is much thinner than  $R_1$ , this occurs at the spinodal pressure given by

$$P_{\text{sp}} = P_{\text{sv}} \cdot \exp\left(-\frac{\gamma V_{\text{mol}}^1}{R_0 \cdot RT}\right) < P_{\text{sv}}, \quad (2.3)$$

since the curvature of the menicus is

$$\zeta = \frac{1}{R_0}.$$

The evaporation process that occurs at equilibrium pressure is the same as for the closed pore.

Important is the inequality

$$P_{\text{eq}}(d) < P_{\text{sp}}(d) < P_{\text{sv}}. \quad (2.4)$$

Figure 2.2 shows the relative vapor pressure to diameter conversion for the equilibrium and the spinodal mechanisms. The conversion is valid for pores of large diameters in which the thickness of the liquid film is negligible. For smaller pores, where the film's thickness becomes relevant, the theory of SAAM and COLE has to be used rather than KELVIN equation.

Qualitatively, the pressures at which condensation and evaporation occur are shifted towards smaller values due to the reduction of the effective pore diameter by the liquid film. (REFHERE???) For even smaller pores, thermal activation may be so important that the hysteresis disappears (REFHERE???).

The long term goal of the team's experiments is to probe these absorption and desorption models. However, for the native pores of 40 nm to 60 nm diameter that are used for the conducted experiments, these effects are believed to be small and the KELVIN equation will be used to translate the condensation and evaporation pressures to pore diameters.

## **2.3 Condensation and evaporation in non ideal pores**

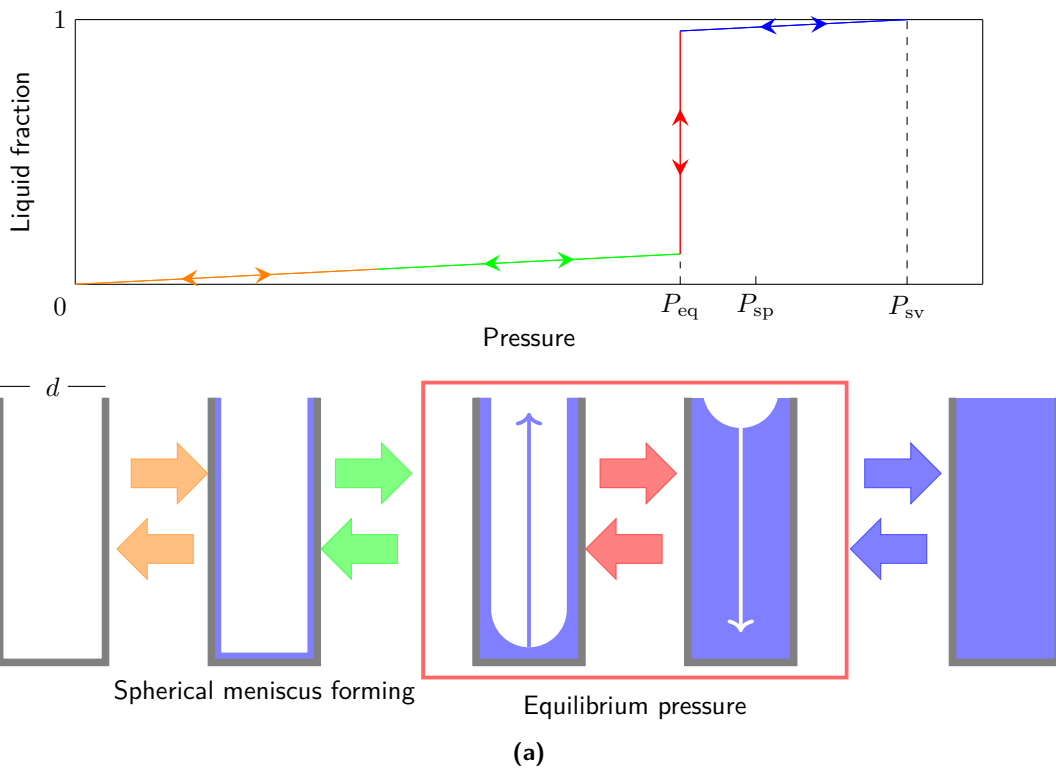
To discuss the condensation and evaporation of hexane in the alumina membranes, the processes must be clear for a single pore. The following explanation starts with a straight cylindrical closed pore. Then, the diameter gradient along the pore's length is added (funnellization). Finally, open pores (straight and funnelled) are discussed.

### **2.3.1 Condensation and evaporation in a closed straight pore**

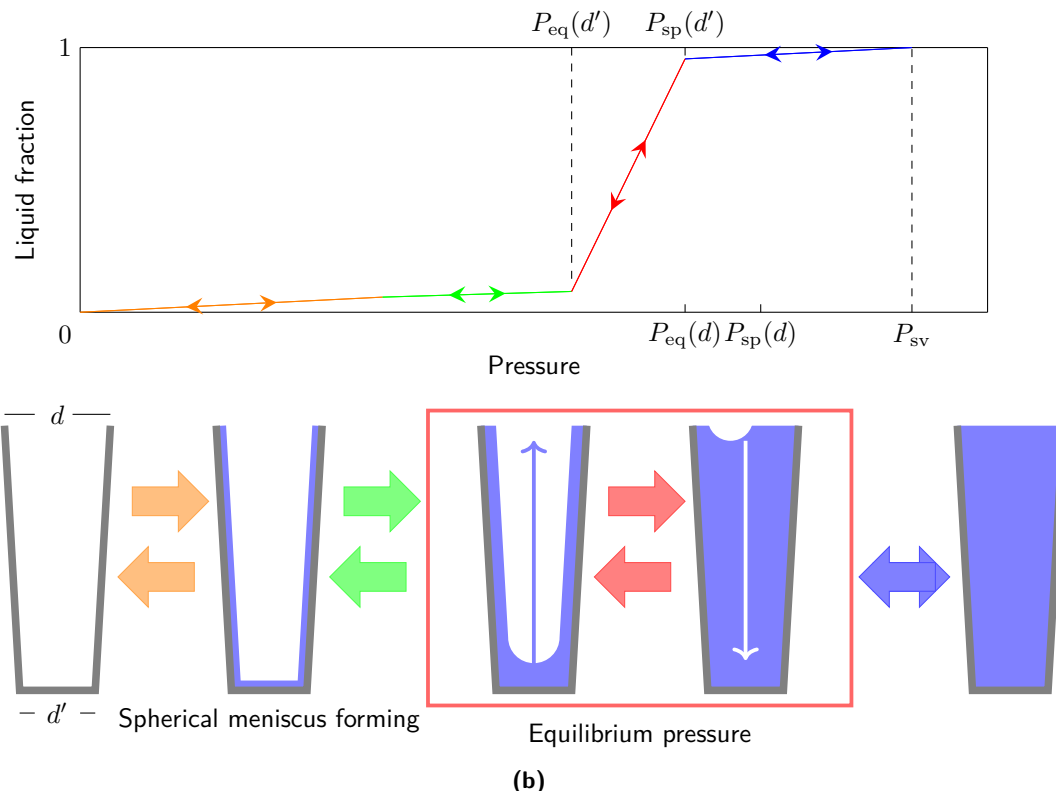
The isotherm for a straight cylindrical pore is illustrated in fig. 2.3(a) with the corresponding processes inside the pore. Exposing the pore to vapor yields a wetting film on its surface (orange pressure range of the isotherm). The film starts forming a spherical meniscus at the closed end of the pore (green). Upon reaching equilibrium pressure  $P_{\text{eq}}(d)$  (compare eq. (2.2)) the pore fills, due to the translational symmetry of the pore, leaving only a spherical meniscus at the open end (red). The latter flattens with increasing pressure till an even surface is left at saturated vapor pressure  $P_{\text{sv}}$  (blue). According to section 2.2, this process is reversible. Upon decreasing the pressure, a spherical menicus forms on the surface of the liquid and recedes to the bottom of the pore at equilibrium pressure. The remaining film evaporates, yielding a fully dried pore at zero pressure.

### **2.3.2 Condensation and evaporation in a closed funnelled pore**

As will be discussed in section 4.2.1, the membrane production yields funnelled pores which are open on the large end. As in the closed straight pore (section 2.3.1), the condensation and evaporation of liquid in a closed funnelled pore is reversible. The difference is that both processes are continuous now: The pore fills and empties over a pressure range depending on the difference between the pore diameters of the top and bottom side. This makes for an inclined isotherm, as can be seen on fig. 2.3(b).

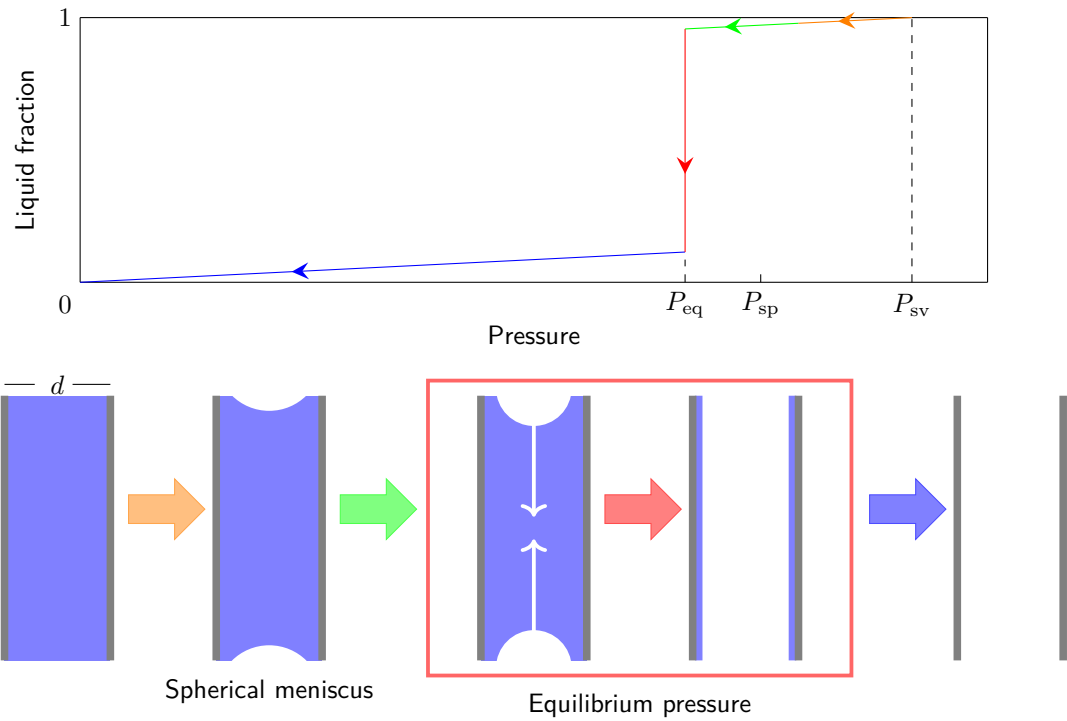
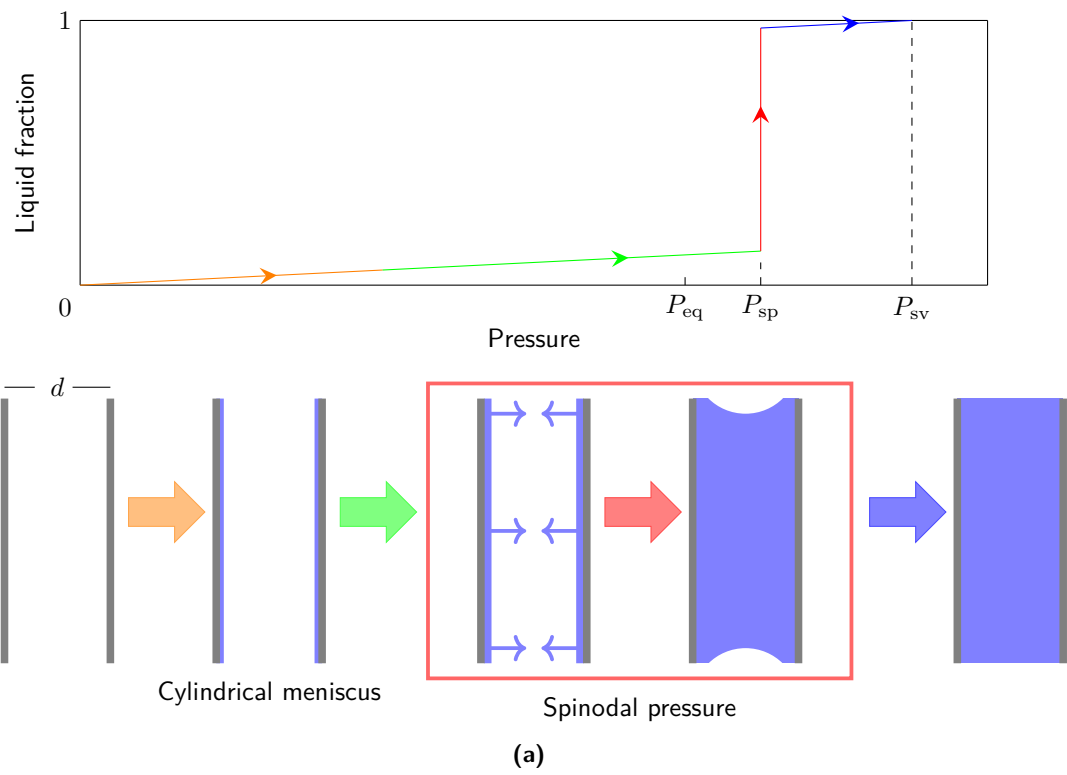


(a)



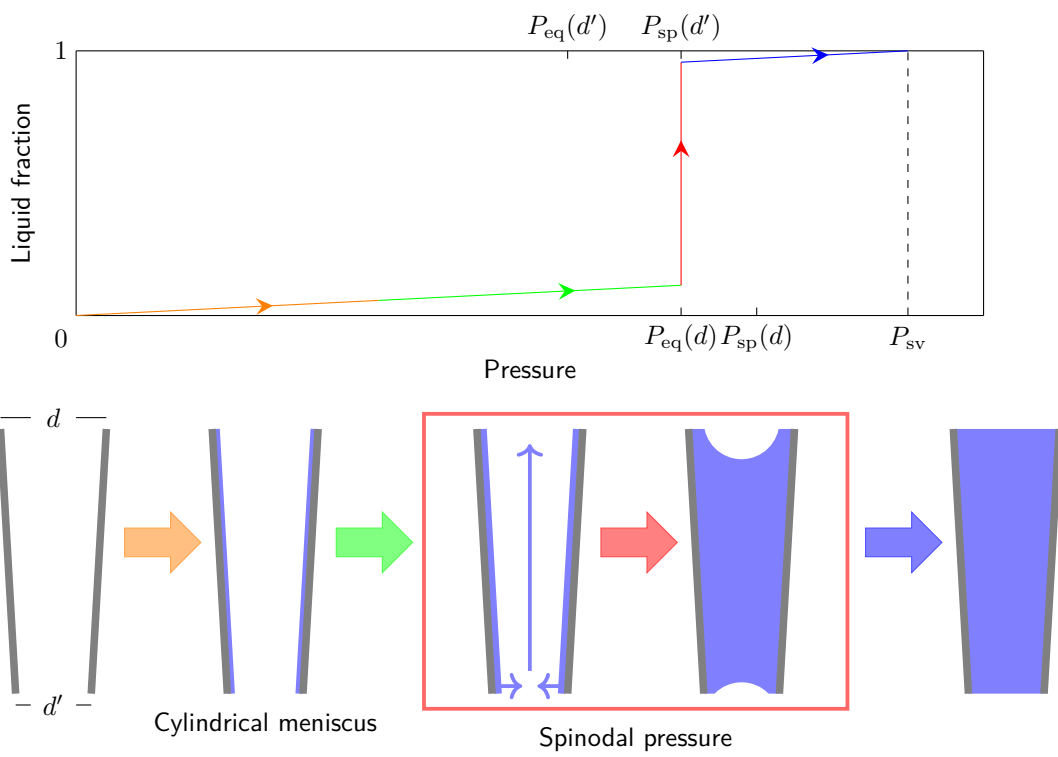
(b)

**Figure 2.3** Condensation and evaporation isotherm model of a closed cylindrical pore. (a) corresponds to the mechanisms in a straight pore whereas (b) does for a funnelled one. The corresponding processes inside the pore are illustrated below the isotherm itself. Colors of the arrows between pore states and the respecting pressure range of the graph match.

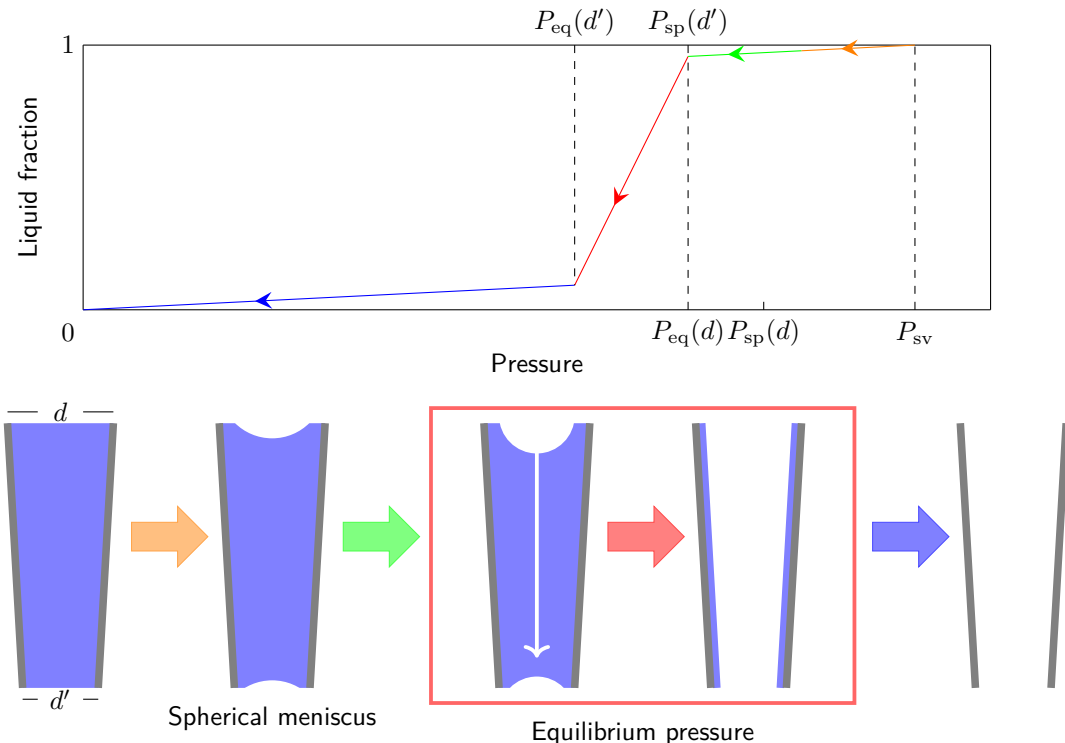


(b) Desorption isotherm. Significant is the desorption at equilibrium pressure.

**Figure 2.4** Condensation (a) and evaporation (b) isotherm of an open straight pore. The corresponding processes inside the pore are illustrated below the isotherm itself. Colors of the arrows between pore states and the respecting pressure range of the graph match.



(a) Absorption isotherm. Significant is the absorption at spinodal pressure  $P_{\text{sp}}(d') \geq P_{\text{eq}}(d)$ .



(b) Desorption isotherm. Significant is the continuous desorption at the equilibrium pressures  $P_{\text{sp}}(d)$  to  $P_{\text{sp}}(d')$ .

**Figure 2.5** Condensation (a) and evaporation (b) isotherm of an open funnelled pore. The corresponding processes inside the pore are illustrated below the isotherm itself. Colors of the arrows between pore states and the respecting pressure range of the graph match.

### **2.3.3 Condensation and evaporation in an open straight pore**

Figure 2.4(a) shows the condensation isotherm branch of an open straight pore and the corresponding processes inside the pore. As explained above, a wetting film forms on the pores inside. However, for an open pore, the latter forms a cylindrical meniscus. Upon reaching the spinodal pressure  $P_{\text{sp}}(d)$  (compare eq. (2.3)), the film collapses, yielding a filled pore with menisci at either open end (red). Because of eq. (2.4), the menisci are spherical cap menisci and evolve into flat surfaces at saturated vapor pressure (blue).

The desorption isotherm for a straight open pore is illustrated in fig. 2.4(b). The only difference with respect to the closed pore is that spherical menisci form on both ends of the open pore. The evaporation of liquid from an open, straight pore works the same as for a closed, straight pore which is described in section 2.3.1.

Thus, condensation and evaporation occur at two different pressures yielding a hysteresis. A complete isothermal loop of condensation and evaporation is shown in fig. 2.6(b).

### **2.3.4 Condensation and evaporation in an open funnelled pore**

Here, an open funnelled pore is regarded. The behaviour for the evaporation is the same as for the closed funnelled pore. It starts at equilibrium pressure of the large end  $P_{\text{eq}}(d)$  from where the meniscus then descends to the smaller bottom end. In contrast, the behaviour for condensation is different. If the funnelling is small enough with respect to the pore's diameter for

$$P_{\text{sp}}(d') \geq P_{\text{eq}}(d).$$

to hold, the pore fills abruptly at spinodal pressure  $P_{\text{sp}}(d')$ . This is the case shown in fig. 2.5(a) and fig. 2.6(b).

For stronger funnelling, the condensation branch of the isotherm shows a vertical rise, followed by a continuous increase due to the further condensation at equilibrium pressure and according to the increasing pore diameter.

Figure 2.6 summarizes the results. A hysteresis occurs only for open pores. Moreover, the funnelling causes an inclined evaporation branch. For a closed pore, the steepness of the condensation branch changes too. In contrast, the condensation branch of an open pore is not affected by the funnelling.

## **2.4 Transmission of a nanoporous alumina membrane**

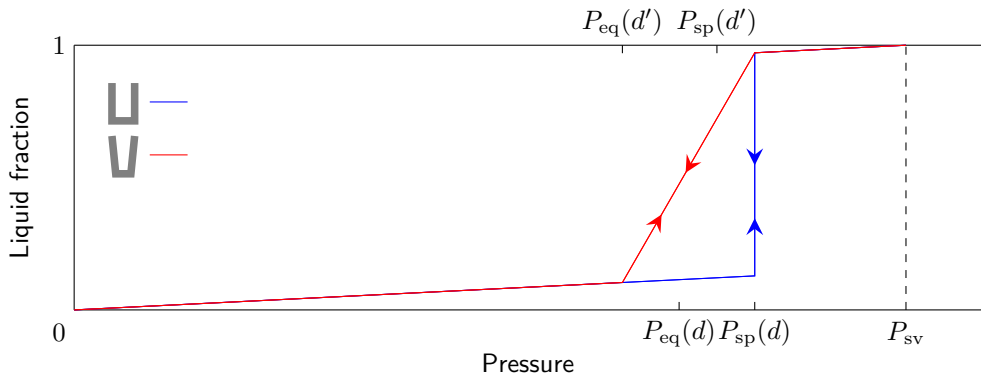
The experimental setup includes laser transmission measurements of the nanoporous alumina membranes. Therefore, the expected FRESNEL transmission coefficients of the membranes in dry state and also with hexane condensed inside the pores are of interest. To keep things simple, the effective medium approximation (compare section 2.4.1) will be used.

### **2.4.1 Effective medium approximation**

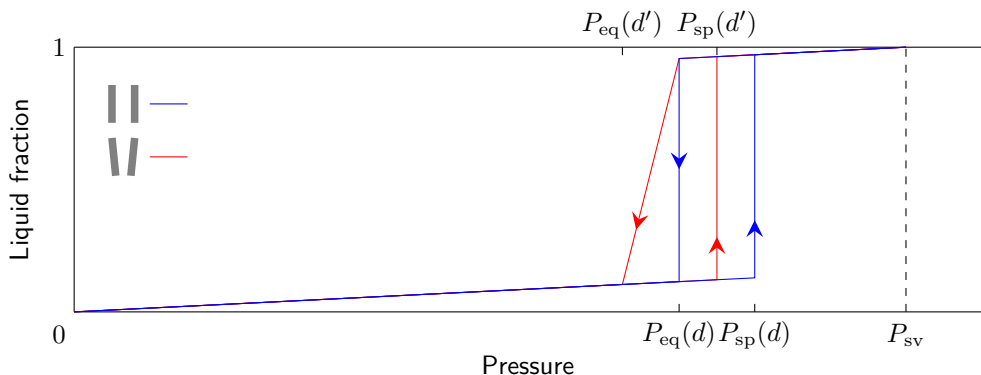
For a medium composed of two components (indice 1 and 2), with the respective fractions  $1 - \phi$  and  $\phi$  and refractive indice  $n_1$  and  $n_2$ , the effective refractive index can be obtained by the effective medium approximation

$$n_{\text{eff}} = n_1 (1 - \phi) + n_2 \phi. \quad (2.5)$$

A visual illustration of the idea is given by fig. 2.7.



(a) Cylindrical pore open on one end.



(b) Cylindrical pore open on both ends.

**Figure 2.6** Absorption and desorption isotherm loops for closed pores (a) and open pores (b). For the funnelled pores it is  $d > d'$ .

#### 2.4.2 Fresnel transmission coefficient of nanoporous alumina membranes

According to (REF NIST???), the refractive indice of alumina and hexane are

$$n_{\text{alumina}} = 1,7682$$

$$n_{\text{hexane}} = 1,3758.$$

Using the FRESNEL formula

$$T = \underbrace{\left( \frac{2n_1 n_2}{n_1 + n_2} \right)^2}_{\text{entering medium 2}} \cdot \underbrace{\left( \frac{2n_1 n_2}{n_1 + n_2} \right)^2}_{\text{reentering medium 2}}$$

and combining with eq. (2.5) yields the transmission coefficients

$$T_{\text{empty}} = 0,92 \quad (2.6)$$

$$T_{\text{filled}} = 0,98. \quad (2.7)$$

#### 2.5 Light scattering in alumina membranes

As will be observed during the experiment, the transmission of the nanoporous alumina membranes is stronger when the pores are filled with hexane than it is in the empty state of the membranes. Furthermore, a transmission drop during the transission from the empty state to the filled state and visa versa will be measured.

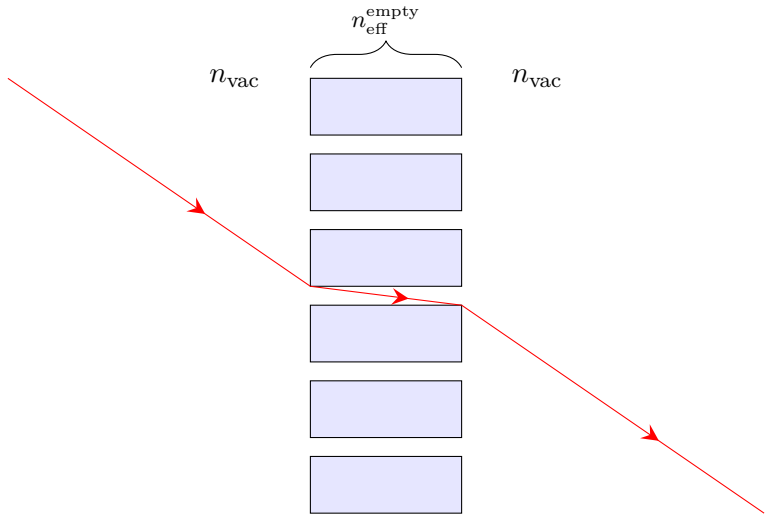


**Figure 2.7** Illustration of the idea behind the effective medium approximation applied on the refractive index of a porous medium (compare section 2.4.1).

The idea behind these phenomena is that the cylindrical pores scatter light. Referring to the theory of RAYLEIGH scattering, this explains the higher transmission values for the filled state of the membranes by index matching. On the other hand, the pores show the order of a hexagonal lattice. If the order were perfect, the membrane should not scatter light, in either empty state or filled, because the distance between pores is small in respect to the wavelength of the light (red light, as a HeNe laser is used). However, the lattice is not perfect, which causes some scattering in both states of the membrane. If now, all the pores do not fill and empty at the same pressures, the optical heterogeneity will increase during the condensation and evaporation process. This causes stronger light scattering and therefore transmission drops during the condensation and evaporation process. The extreme magnitude of these drops can be explained by the large length of the pores.

## 3 Experimental

### 3.1 Membrane production

The alumina membrane production process starts with a circular wafer of amorphous aluminum of 99,999 % purity and 1 mm thickness. In a first anodizing step, parallel pores are created that show a hexagonal order (section 3.1.1). Then, the remaining aluminum of the wafer is dissolved by immersion in an acid as specified in eq. (3.1) in section 3.1.2. Next, the so called *barrier layer* closing the pores on the bottom end is etched by floating the wafer on oxalic acid (section 3.1.3). Last, the pore diameters are reduced using atomic layer deposition (ALD).

With an initial diameter of  $d_{\text{wafer}} = 5 \text{ cm}$ , one wafer is broken into twelve square membranes, the side length being  $l_{\text{membrane}} = 1 \text{ cm}$ . Since the wafer has a thickness of  $l_{\text{pore}} = 30 \mu\text{m}$  to  $60 \mu\text{m}$ , the wafer is precut using a scalpell before the anodization. This step enables to cleave the wafer easily. As the cleaving step is performed at the very end of the membrane synthesis, the square membranes are expected to show equivalent characteristics.

#### 3.1.1 Anodizing

Figure 3.1 shows a sketch of the anodizing setup. The bulk aluminum wafer (compare fig. 3.2(a)), which functions as the anode, is glued to a copper plate using conductive silver paste. The copper plate is then covered by non conductive polymer CAF4 leaving only the circular surface of the wafer exposed to the acid. A platinum plate that is placed at a horizontal distance of 3 cm from the anode functions as cathode. The whole setup is immersed in oxalic acid that is continuously stirred. The anodization is conducted at a constant voltage  $U_{\text{anodizing}}$ .

The pore diameter  $d_{\text{pore}}$  and the inter pore distance  $d_{\text{interpore}}$  depend on the anodizing conditions. Along with  $U_{\text{anodizing}}$ , these are given by the oxalic acid's molar concentration  $n_{\text{C}_2\text{H}_2\text{O}_4}$  and its acid temperature  $T_{\text{C}_2\text{H}_2\text{O}_4}$ . Their variation changes the pore diameters between 10 nm and 100 nm. To produce wafers with the pore specifications

$$d_{\text{pore}} = 40 \text{ nm}, \\ d_{\text{interpore}} = 100 \text{ nm},$$

the anodization is conducted using the parameters

$$U_{\text{anodizing}}^{40 \text{ nm}} = 40 \text{ V}, \\ n_{\text{C}_2\text{H}_2\text{O}_4} = 0,5 \frac{\text{mol}}{\text{l}}, \\ T_{\text{C}_2\text{H}_2\text{O}_4} = 15^\circ\text{C}.$$

This makes for a growth rate of alumina of

$$r_{\text{Al}_2\text{O}_3} \approx 8 \frac{\mu\text{m}}{\text{s}}.$$

To ensure that parallel pores are produced, a two step anodization procedure is followed.

The first anodizing treats the raw bulk aluminum wafer. By the oxalic acid  $\text{C}_2\text{H}_2\text{O}_4$ , pathways are etched into the aluminum which follow no pattern at first. Only some of them continue to grow

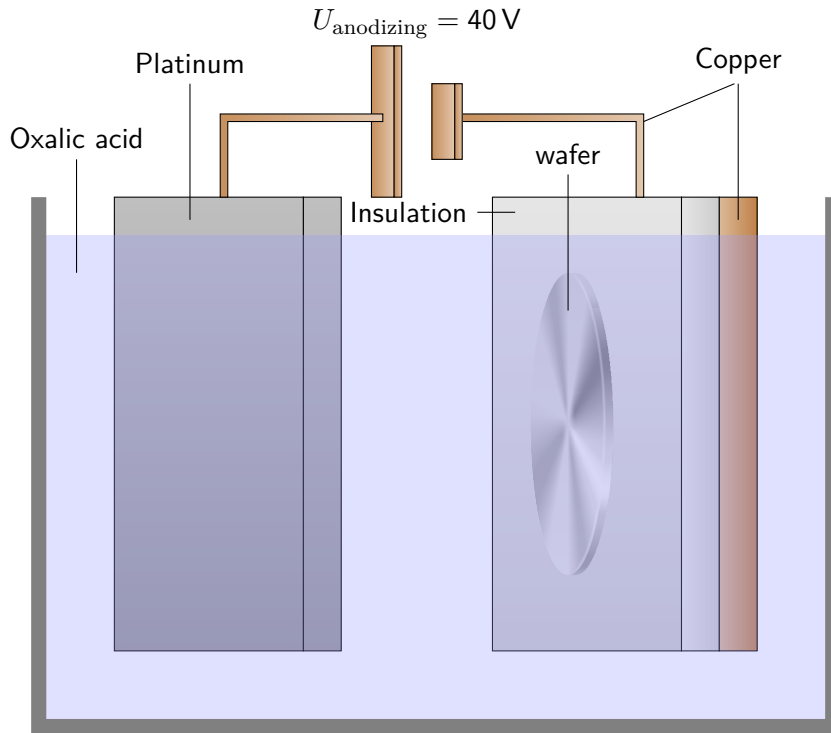


**Figure 3.1** Setup for the anodizing of the membrane production. The aluminum wafer functions as anode while a platinum plate makes for the cathode. The oxalic acid is stirred during the whole process.

forming real pores, though. With the ongoing anodizing, pores start to combine to form larger pores and finally areas of hexagonally arranged pores are created throughout the wafer. The longer the anodizing process is carried out, the wider these ordered areas become. Figure fig. 3.2(b) shows the cross-section of a wafer observable at this point. Because the process transforms aluminum to alumina at a given penetration speed, the so called *barrier layer* of alumina separates the pores from the bulk aluminum.

Before the second anodizing, the wafer is immersed in a mixture of chromic and phosphoric acid with the concentrations

$$n_{\text{H}_3\text{PO}_4} = 0,4 \frac{\text{mol}}{\text{l}}$$

$$n_{\text{CrO}_3} = 0,2 \frac{\text{mol}}{\text{l}}$$

at a temperature of

$$T_{\text{CrO}_3}^{\text{H}_3\text{PO}_4} = 0,2 \frac{\text{mol}}{\text{l}}.$$

Hereby the created alumina is dissolved yielding a slightly thinner wafer of bulk aluminum, where the thickness  $d'_{\text{Al}}$  depends on the time of the first anodizing. The relevant difference to the initial wafer are the areas of hexagonally arranged hollows (compare figure fig. 3.2(c)).

Due to this new surface structure, the second anodizing yields a wafer with a top layer of alumina penetrated by parallel, hexagonally arranged pores. Again, the *barrier layer* of alumina separates the pores from the bulk aluminum as illustrated in figure fig. 3.2(d). Increasing the time of the second anodizing increases the length of the pores  $l_{\text{pore}}$  and hereby the thickness of the final wafer. As the second anodizing is carried out under the same conditions as the first, the pore size  $d_{\text{pore}}$  is the same in both production steps.

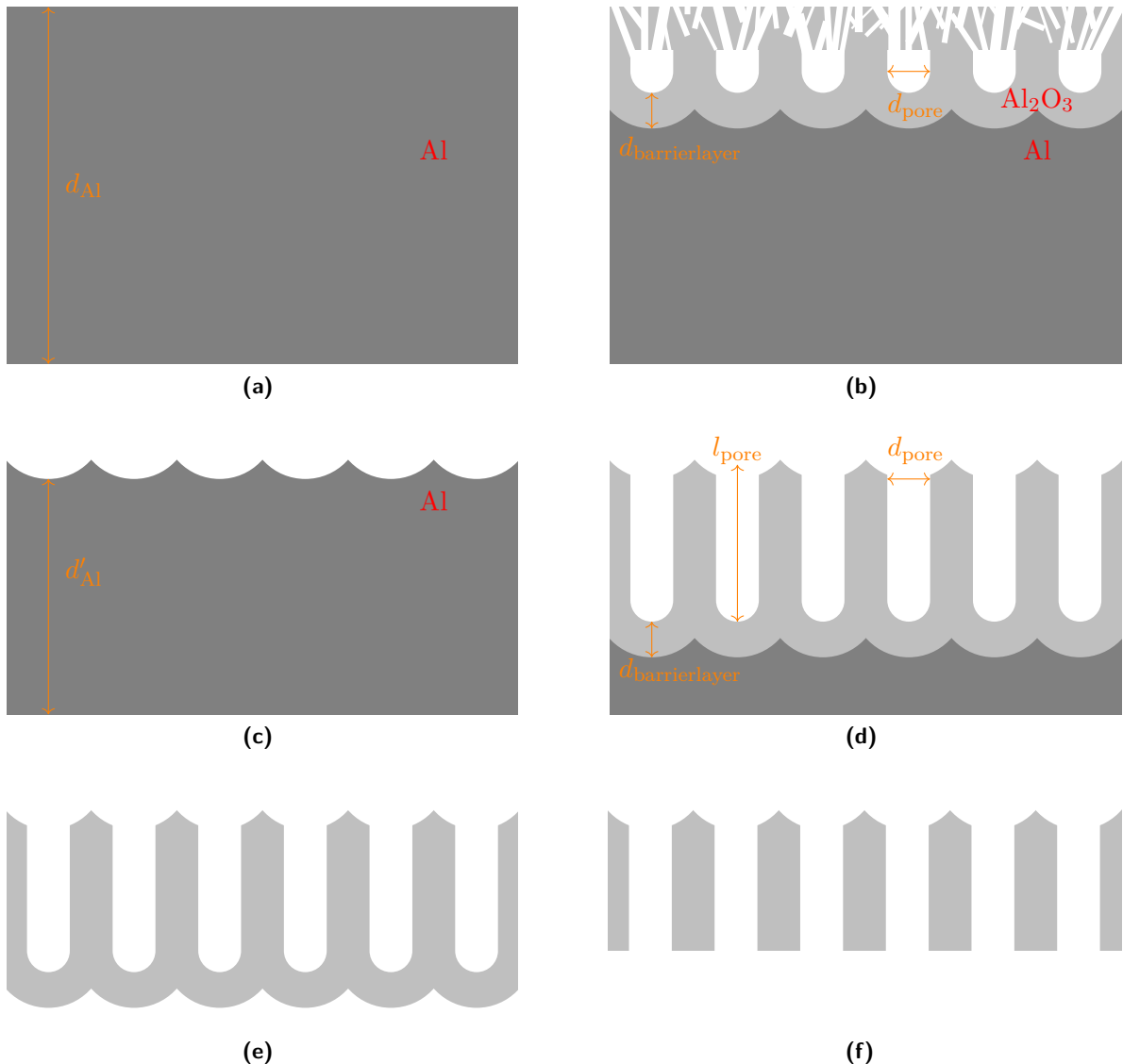
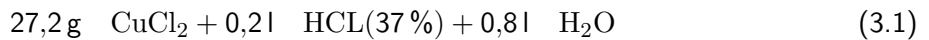


**Figure 3.2** Production stages of the membrane production. It starts with a wafer of bulk aluminum (dark gray) (a) which is then anodized yielding (b), where light gray represents alumina. The latter is then dissolved producing a bulk aluminum wafer with hexagonally arranged hollows (c). By the second anodizing, straight parallel pores are created (d). After dissolving the remaining aluminum (e), the barrier layer etched to open the pores (f). The initial aluminum wafer's thickness is  $d_{\text{Al}} = 1 \text{ mm}$ , the *barrier layer* thickness  $d_{\text{barrier-layer}}$  is 30 nm to 60 nm, the pore diameters  $d_{\text{pore}} = 10 \text{ nm to } 100 \text{ nm}$  and the pore length or membrane thickness  $l_{\text{pore}} = 30 \mu\text{m to } 60 \mu\text{m}$ .

### 3.1.2 Aluminum dissolution

To dissolve the remaining aluminum on the bottom side of the wafer, it is immersed in an acid composed of



at a temperature of

$$T = 0^\circ\text{C} \quad (3.2)$$

as shown in figure fig. 3.3(a). The latter transforms the aluminum to copper in a very exothermic reaction. A lot of turbulences are created and thus this step limits either the thickness or the size of the wafers because they can easily break.

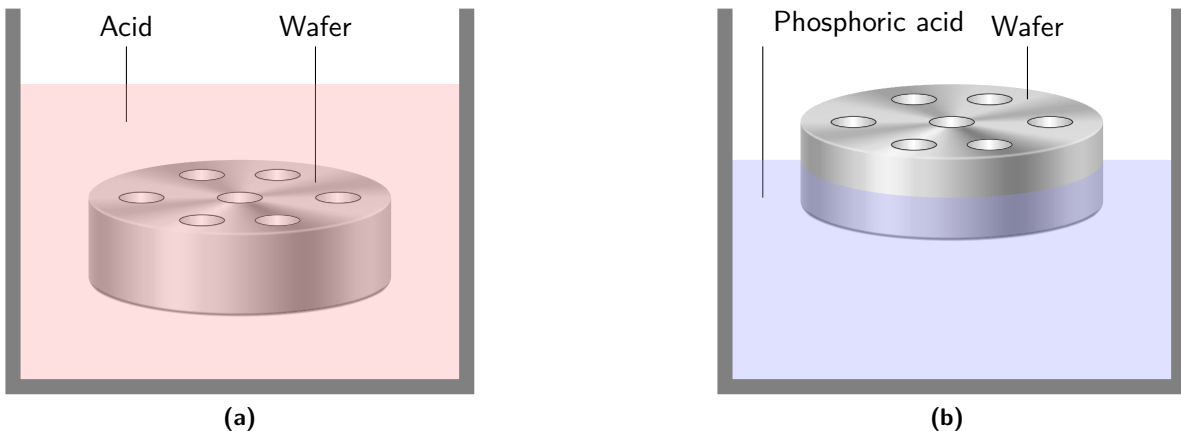


**Figure 3.3** (a) shows the setup for the aluminum dissolution step. The wafer is immersed in acid composed according to eq. (3.1) which dissolves aluminum. In (b) the *barrier layer* dissolution by floating the membrane on phosphoric acid is illustrated.

### 3.1.3 Barrier layer dissolution

The *barrier layer* dissolution is done using phosphoric acid of the concentration

$$n_{\text{H}_3\text{O}_4\text{P}} = 0,2 \frac{\text{mol}}{\text{l}}. \quad (3.3)$$

To dissolve the *barrier layer* and hereby open the pores, the wafers are floated on phosphoric acid as shown in figure fig. 3.3(b). After 15 min to 30 min, the wafer starts showing milky aspects (compare fig. 3.4(a)). This is due to opening pores which fill with acid before others as will be explained in more detail in section 4.3. The phenomenon lasts for about

$$t_{\text{milky}} = 3 \text{ min} \quad (3.4)$$

before they disappear and the wafer becomes transparent again. From this point, the new wafers (295 and 296 with more to come) are floated for 15 min more to ensure well open pores (in contrast to bad open pores, which will be discussed in section 4.3.1). Just before removing the wafers from the phosphoric acid, a liquid film covers their whole surface as photographed in fig. 3.4(b).

### 3.1.4 Atomic layer deposition

Atomic layer deposition (ALD) is a thin film deposition method. Figure 3.5 illustrates the following explications. Within a reaction chamber, the substrate is exposed to a first precursor (red in fig. 3.5(a)). This precursor coats the substrate with a monolayer of molecules in a self limited reaction. When the whole substrate is covered, no reactive sites remain and therefore no more molecules are deposited. Upon evacuation of the reaction chamber, the monolayer remains on the substrate (compare fig. 3.5(b)), which is then exposed to a second precursor (fig. 3.5(c)). Like the first one, this second precursor covers the substrate's surface with a monolayer of molecules (fig. 3.5(d)). This process is repeated until the desired thickness of deposition on the substrate has been reached (fig. 3.5(e) and (f)). Fundamental for the ALD process is that the two precursors are reactants.

For the ALD on the alumina membranes the reaction chamber is heated to

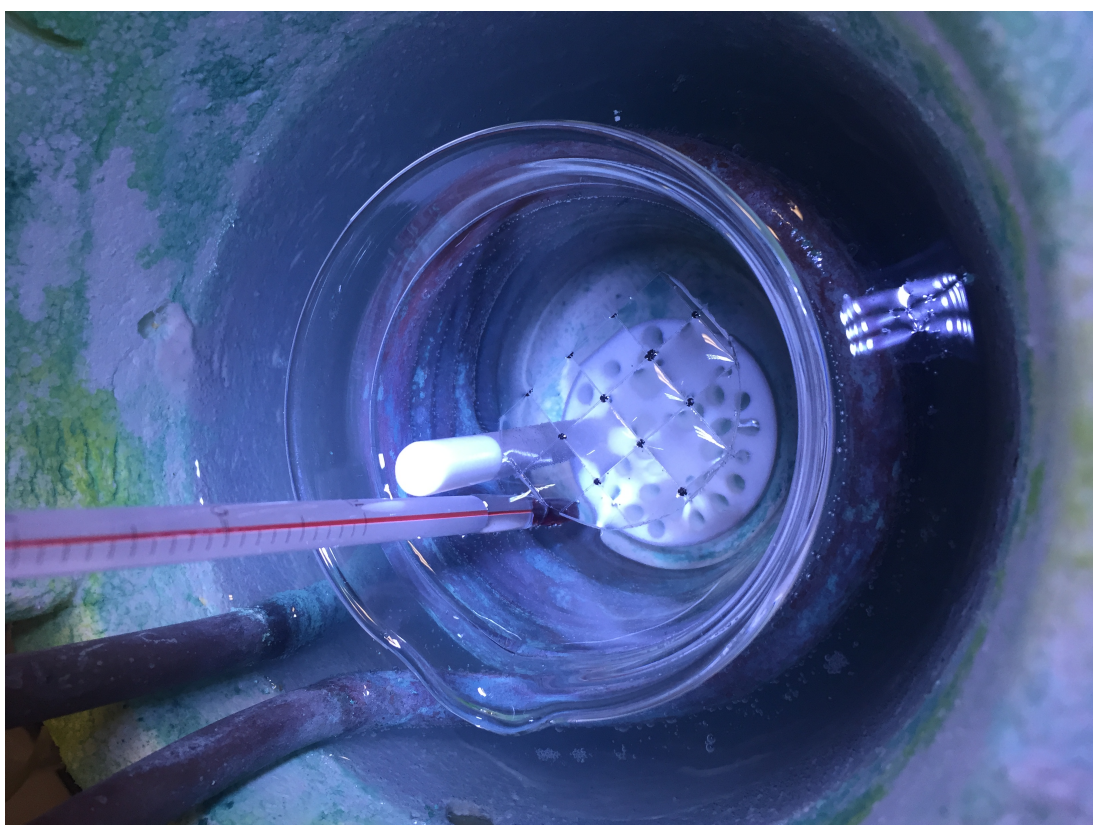
$$T_{\text{reaction-chamber}} = 200^\circ\text{C}.$$

The used precursors are trimethylaluminium (TMA) and water. This makes for an expected growth rate of

$$g_{\text{ALD}} = 1,2 \text{ \AA}$$



(a)



(b)

**Figure 3.4** Photos taken during the *barrier layer* dissolution step. (a) shows the milky aspects that appear during the floating of the wafers. In (b), a film of phosphoric acid covers the whole wafer at the end of the process.

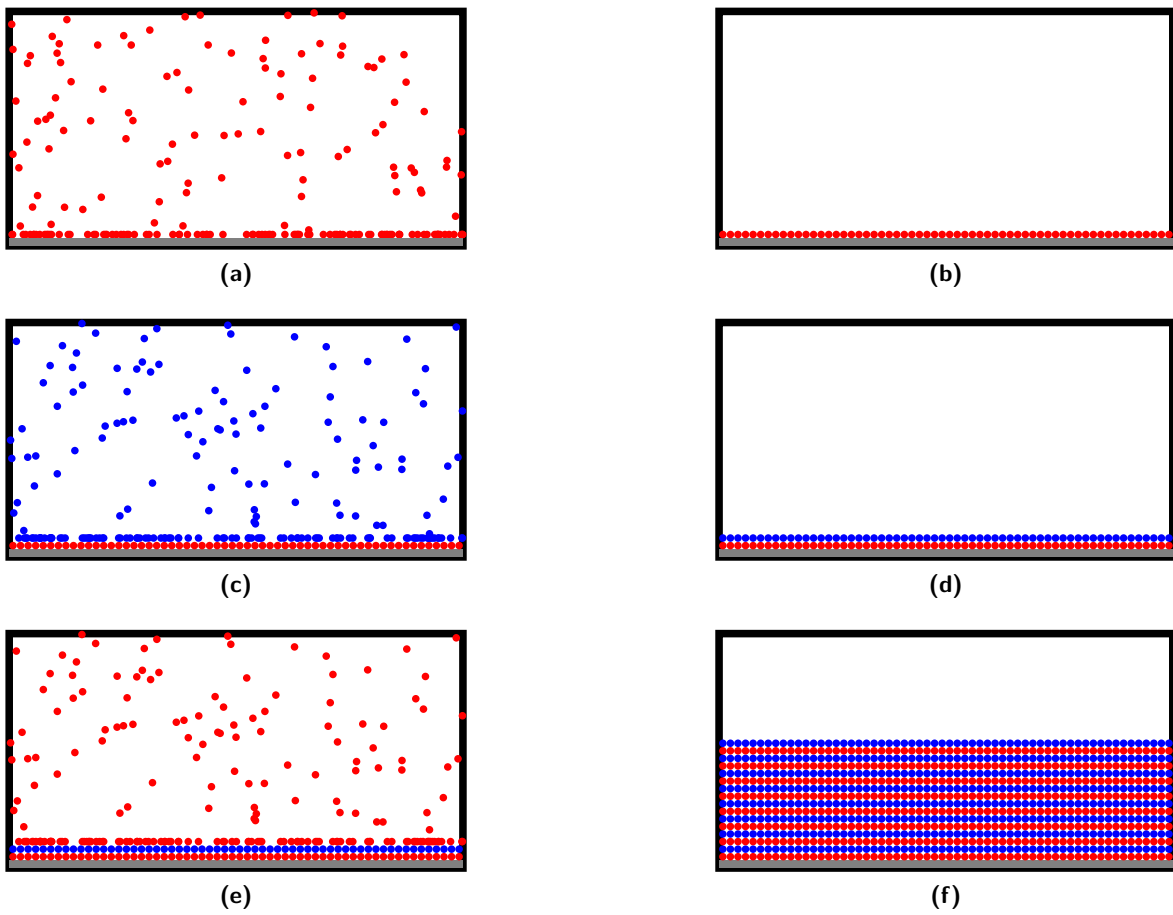


**Figure 3.5** Illustration of the atomic layer deposition process. For explanations please refer to section 3.1.4.

per cycle. REF??? Since in this experiment the ALD process is used to reduce the pore diameters of the pores, the expected reduction rate of the pores is

$$\delta d_{\text{pore}} = 2,4 \text{ \AA}.$$

### 3.1.5 Terminology

In the course of this article, the term *solution side* refers to the surface of the membranes that has been anodized according to section 3.1.1. The *aluminum side* is the opposite side of the membranes that is still covered by aluminum after the anodization procedure. Furthermore, the *top end of a pore* is on the *solution side*, whereas the *bottom end of a pore* corresponds to the *aluminum side*.

## 3.2 Scanning electron microscopy

Scanning electron microscopy (SEM) is used to characterize the nanoporous alumina membranes. While the measurements are very fast in comparison to the isotherm measurements, SEM is destructive and yields the pore diameters with limited precision.

To start with, as alumina is a non conductive material, a conductor must be deposited on the membranes' surfaces. In *Institut Néel*, gold is used to this end. This process does not only reduce the diameters of the pores, but also destroys the membranes. The slight constriction the gold forms at the end of the pores changes the isotherms and moreover, the membranes are not transparent to red light anymore, which prevents further transmission measurements.

Generally, the SEM only records images of the membranes' surfaces. Since the pores' length is three orders larger in magnitude than the pores' diameter, the acquired information does not serve for a precise characterisation of the pores' shapes.

Moreover, the porosity of the membranes is not known and thus, the threshold of the binarisation of the images that is done in the course of the diameter extraction. In conclusion, the measured pore diameters are rather uncertain.

### 3.2.1 Statistical evaluation of the SEM images

In the course of the internship, I programmed a statistical analysis of the SEM images with the possibility to either use the mean gray intensity or a manual set threshold for the image binarisation. From the binary files, the largest inscribed circle is computed for every pore. This data is then plotted on a histogram that also evaluates the circularity of the pores. The largest inscribed circle is used because the liquid film tends to form a circular meniscus within the pore due to the stresses implied by different meniscus curvatures (compare LAPLACE-YOUNG equation). These results are then to be compared to the diameters derived from the condensation and evaporation models.

## 3.3 Experimental setup

The experimental setup consists of two independent parts. To record isotherms, the core of the experiment is the volumetric measurement conducted in the setup explained in section 3.3.1. In addition to that, there are a light transmission setup and a camera setup that can be set up one at a time. Both setups are used to monitor what happens during the absorption and desorption isotherms using optics. While the camera setup accumulates data for the whole surface of the membrane, the light transmission measurement probes a small area of the membrane. Both methods are used to measure the heterogeneities of the processes of condensation and evaporation and to put them in context with the volumetric isotherms. The advantage of the laser transmission measurement is the ease of the data evaluation.

### 3.3.1 Volumetric setup

The initial volumetric setup is sketched in fig. 3.7. A reservoir of liquid hexane immersed in a thermostatted bath (LAUDA) at a controlled temperature  $T_{\text{bath}}$  acts as a source of hexane gas. The dependency of the vapor pressure  $P_v$  on the bath's temperature  $T_{\text{bath}}$  is given by ANTOINE equation (REF???)

$$P_v = 10^{A - \frac{B}{C + T_{\text{bath}}}}, \quad (3.5)$$

which is plotted for hexane in the relevant temperature range in fig. 3.6 using the ANTOINE equation parameters

$$\begin{aligned} A &= 4,00266, \\ B &= 1171,53, \\ C &= -48.784. \end{aligned} \quad (3.6)$$

This reservoir is connected to the rest of the experiment by a valve. Behind the valve lies a cross leading to a pressure gauge  $P_{\text{res}}$ , via another valve to a primary pump (void), and via a PFEIFFER EVR116 needle microvalve to the cell containing the sample membrane. This branch is also connected to a pressure gauge  $P_{\text{cell}}$ . The microvalve is the key part of the experiment as it allows for the extremely low flow rates that are necessary for the conducted experiment (section 3.4).

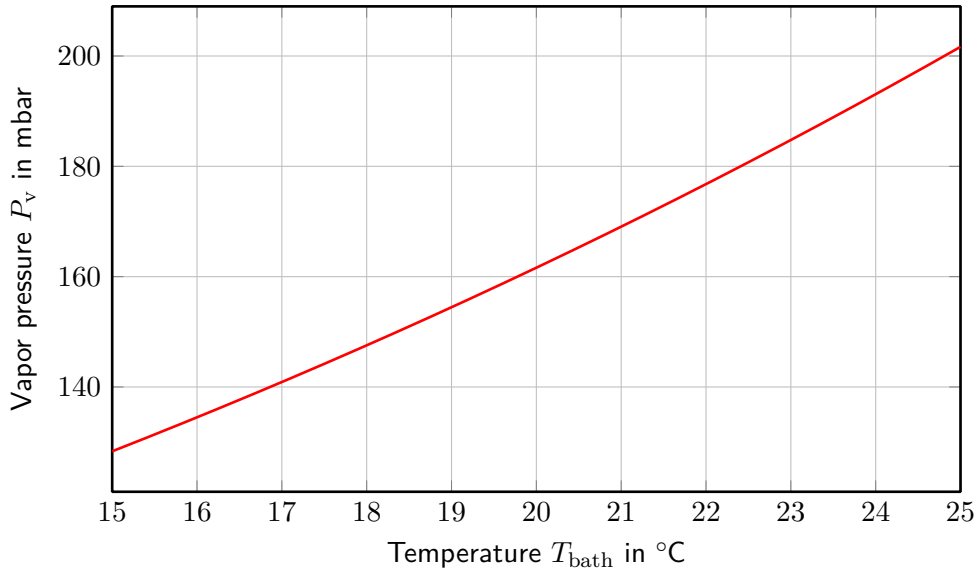


**Figure 3.6** Vapor pressure of hexane according to ANTOINE equation (eq. (3.5)) using the ANTOINE equation parameter eq. (3.6) for hexane.

Furthermore, the temperature of the cell and that of the thermostatted bath are monitored by the thermometers  $T_{\text{cell}}$  and  $T_{\text{res}}$ .

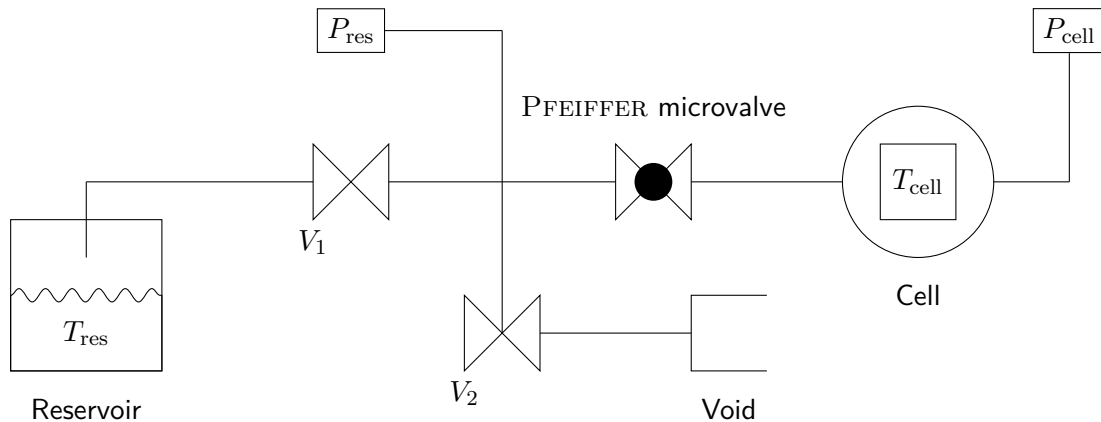


**Figure 3.7** Experiment setup. The temperatures within the reservoir and the cell are measured by the thermometers  $T_{\text{res}}$  and  $T_{\text{cell}}$ . Furthermore,  $P_{\text{res}}$  and  $P_{\text{cell}}$  are the two installed pressure gauges. The void is experimentally realized by a primary pump.

The whole experiment setup is placed in a climatized room set to

$$T_{\text{room}} = 23^{\circ}\text{C}. \quad (3.7)$$

The coldest point of the experiment must be the cell containing the sample membrane as to be sure no hexane condenses anywhere else in the setup. Therefore, the temperature of the cell is regulated to

$$T_{\text{cell}} = 19^{\circ}\text{C} \quad (3.8)$$

as mentioned in section 3.3.1.1. The the reservoir of bulk hexane is set to a temperature of

$$T_{\text{res}} = 21^{\circ}\text{C} \quad (3.9)$$

using the LAUDA allowing to fully condense the cell at  $T_{\text{cell}}$ .

### 3.3.1.1 Cell temperature regulation

The cell itself is made of a copper ring which is sealed on both sides using sapphire windows. Making use of indium O-rings, the windows are pressed onto the copper ring by two stainless steel rings. This circular cell is designed so it can be inserted in a copper clamp which is connected to a PELTIER heat pump and a heater. Moreover, two thermometers are installed - one for the temperature regulation feedback loop and one for the output value. While the power of the PELTIER is fixed, the heater's power output is controlled by the feedback loop. From the microvalve to the pressure gauge  $P_{\text{cell}}$ , the setup is packed in styrofoam for thermal insulation from the room temperature and also to minimize the gradient inside this part of the setup. At first, the regulation has been run via a regular computer. As this led to breakdowns of the regulation for short periods of time multiple times per hour, the regulation was then externalized to a RASPBERRY PI. It regulates the temperature to  $T_{\text{cell}} = 19,000(5) \text{ }^{\circ}\text{C}$ .

### 3.3.1.2 Pressure gauges

Because of its high resolution, a KELLER pressure gauge was used for  $P_{\text{cell}}$  at first. My first experiments revealed that its construction contains a porous O'ring that could be identified as the source of degassing inside the system. After discussions with the retailers, we chose to swap the pressure gauge for a WIKA S10 which exposes only metallic parts to the hexane.  $P_{\text{res}}$  uses the same model of pressure gauge.

## 3.3.2 Laser transmission setup

The laser transmission setup is sketched out in fig. 3.8. In the path of the initial laser beam, a collimator and a diaphragm are placed before the cell. After being scattered by the membrane, the beam then passes another diaphragm and a collecting lens before hitting the photodiode.

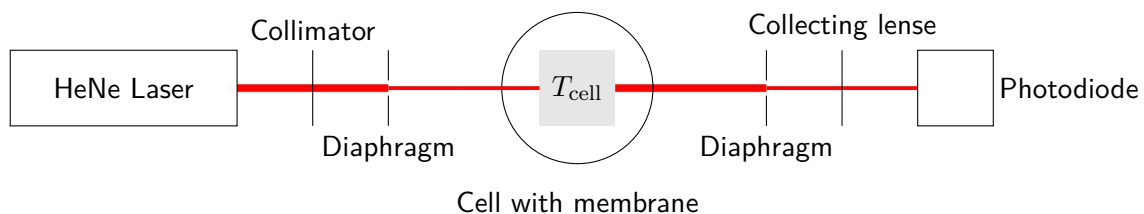


**Figure 3.8** Sketch of the laser transmission setup.

### 3.3.3 Camera setup

To record images of the membranes during the absorption and desorption isotherms, a camera is installed and focused on the alumina membrane. A green LED lamp by THOR LABS is used as a light source. The camera and the light source are positioned on opposite sides of the membrane as to measure the transmission. For the setup, a ZYLA camera by ANDOR is used with a 50 mm makro lens.

## 3.4 Experimental procedure

Only one of the two is set in place at the same time though To start an experiment (here also referred to as an isotherm) the valve  $U_1$  is closed while  $U_2$  and the PFEIFFER microvalve  $U_{\text{PV}}$  are

fully opened. This allows the primary pump, which experimentally realizes the void, to pump the system. After setup has been assembled, the first pumping process serves to clean the system from the air that unavoidably enters the system when placing a membrane inside the cell (or removing it from the cell). After this, the air that enters the system through leaks is pumped in between two isotherm measurements. To start an isotherm after a pumping process,  $U_2$  is closed and the condensation process initialized by setting  $U_{PV}$  to a sufficiently low opening voltage and opening  $U_1$ . Sufficiently low opening voltage shall imply that the condensation plateau of the condensation inside the membrane's pores is distinguishable on the recorded  $P$  over  $t$  isotherm. The employed flow rate's magnitude is  $10^{-5} \frac{\text{mbar}}{\text{s}}$ .

To also record the bulk condensation plateau, which defines the saturated vapor pressure  $P_{sv}$  in the evaluation process, the setup is left condensing inside the cell for five hours after the pressure inside the cell reaches  $P_{cell} = 150 \text{ mbar}$ . This way a small amount of bulk liquid is condensed inside the cell. At the end of the process, all the valves are closed.

The evaporation process is then initialized by opening the valve  $U_2$ . Meanwhile, the PFEIFFER microvalve is set to a sufficiently low opening voltage  $U_{PV}$  to permit the primary pump to pump the system. Again, sufficiently low implies that the evaporation plateau of the liquid evaporating from the membrane's pores is visible on the recorded  $P$  over  $t$  isotherm. The system is left in this state till the pressure inside the cell  $P_{cell}$  reached a given setpoint at which the microvalve is fully opened to pump the system and prepare for another isotherm.

### 3.4.1 Bypass

As the flow rate of hexane in the system depends on the opening of the PFEIFFER microvalve and the pressures  $P_{res}$  and  $P_{cell}$ , this opening should always be the same to be able to compare multiple isotherms. As my experiments raised the suspicion of a hysteresis upon opening and closing of the microvalve, a bypass is added to the setup. Figure 3.9 shows the new setup, which allows to pump the part of the system containing the cell without changing the opening of the PFEIFFER microvalve. This way there is no need to ever change the before and one potential error source is removed from the system.

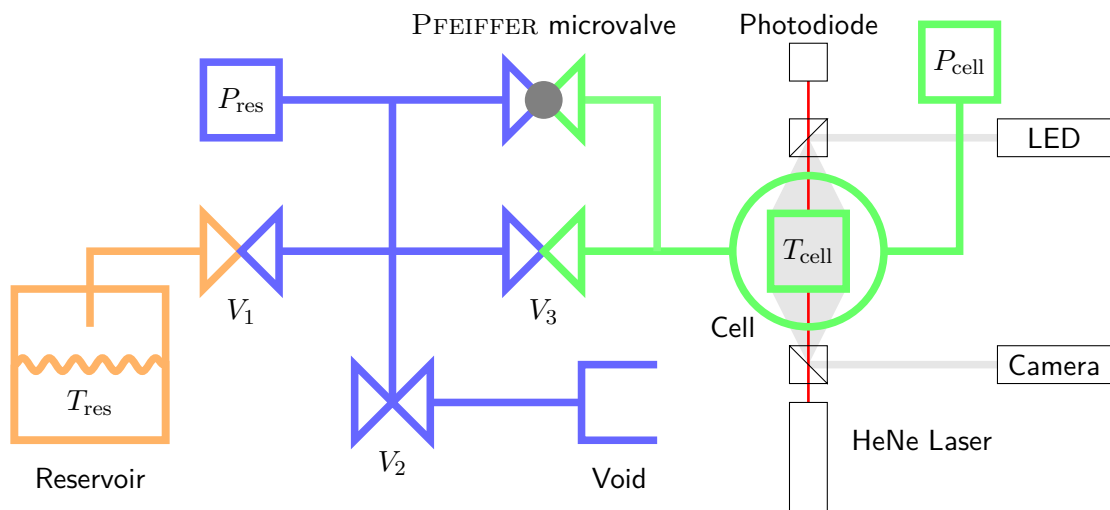


**Figure 3.9** Final experiment setup. With respect to fig. 3.7, the bypass allows to pump the whole system without changing the opening of the PFEIFFER microvalve. Furthermore, the laser transmission setup and the camera setup are outlined.

The green volume of the system, which is the one of interest for the isotherm computation, is calibrated using BOYLE's law. Its volume is approximately

$$V_{cell} = 8,3 \text{ cm.} \quad (3.10)$$

### **3.4.1.1 Changing the membrane**

To change the sample, the copper cell must be opened and therefore detached from the rest of the system. After placing the membrane to be measured inside the cell, the latter is reconnected to the system. As a result, the inside of the cell is at atmospheric pressure. Before the bypass was installed, to pump the cell, the PFEIFFER microvalve had to be opened. Using the small opening also used for the isotherms would have made for an unbearably long pumping process. For an approximation please refer to fig. 3.10(a) in section 3.5.1 where hexane is pumped from the system. As the evaluation of the volumetric measurements depends strongly on the opening of the PFEIFFER microvalve which is not guaranteed to reopen without a hysteresis even if the same voltage as before is applied, the bypass has been installed to create a way to pump the system without touching the PFEIFFER's opening. From this point on, the contamination of the cell with degassing grease and the VCR connectors, that leak a small amount of air into the system, are the most prominent hazards of the membrane changing process.

## **3.5 Isotherm computation**

In the following, evaluation of the recorded raw data is presented for volumetric (section 3.5.1) and for the optical measurements (section 3.5.2).

### **3.5.1 Volumetric isotherm**

The volumetric isotherms are obtained through a calibration of the PFEIFFER needle microvalve. Figure 3.10(a) shows the pressure inside the cell versus time for one measurement without membrane and one with membrane inside the cell. When there is no membrane inside the cell, there is only one bulk condensation and evaporation plateau visible on the curve. In contrast to that, additional condensation and evaporation plateaus appear when there is a membrane inside the cell. These additional plateaus correspond to the dips on the so called *pressure loop* plot displayed in fig. 3.10(b). From here on, the following indices shall be used:

- 1 → no membrane
- 2 → membrane.

Furthermore, the variables  $P_i$ ,  $\dot{P}_i$ ,  $V_i$ ,  $T_i$ ,  $n_i$  and  $\dot{n}_i$ ,  $i \in \{1, 2\}$ , refer to the values measured inside of the cell, in explanation the red marked part of the system in fig. 3.9. The raw isotherms of the two experiments are shown in fig. 3.10. The plateaus of the yellow curve with membrane inside the cell of the plot versus time correspond to the dips of the time derivative of the pressure of the versus pressure plot. This can be explained by the hexane condensing inside the membrane's pores at a given pressure due to which the continuing matter flow into the cell does not yield an increase of pressure.

Regarding the system with an empty cell, the ideal gas law is used to compute the flow rate of hexane. The content of the cell without membrane inside the cell is given by

$$n_1 = \frac{P_1 V_1}{RT_1},$$

taking into account that the temperature of the cell is regulated at  $T_1$  and the volume  $V_1$  is constant, the flow of matter is

$$\dot{n}_1 = \frac{V_1}{RT_1} \cdot \dot{P}_1.$$

For the system with a membrane inside the cell the flow of matter is the sum of the flow into the membrane  $\dot{n}_2^{\text{mem}}$  and the flow into the system volume excluding the membrane  $\dot{n}_2^{\text{cell}}$ . This can be

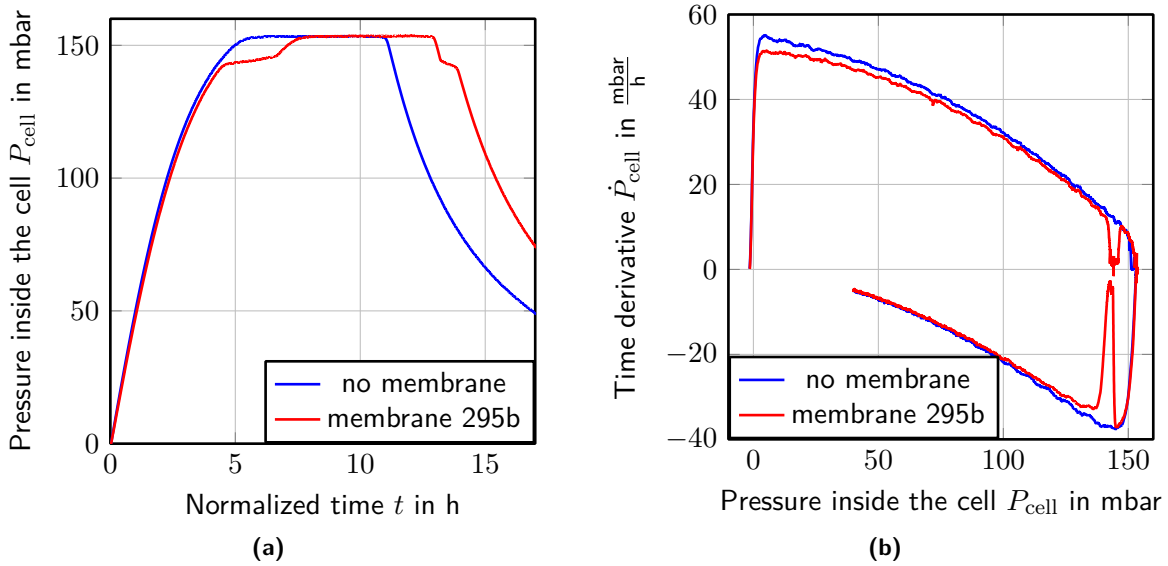


**Figure 3.10** Raw volumetric isotherm data recorded with the experimental setup as explained in section 3.4 for one cycle without a membrane inside the cell and one with a membrane inside the cell. (a) shows the pressure values over time making the condensation and evaporation plateaus of absorption and desorption of hexane within the membrane's pores visible. (b) is the pressure loop which is relevant for the computation of the isotherms. Again, the before mentioned plateaus are visible as dips in the time derivative of the pressure.

rewritten yielding

$$\dot{n}_2^{\text{mem}} = \dot{n}_2 - \dot{n}_2^{\text{cell}},$$

where  $\dot{n}_2^{\text{cell}}$  is given by the ideal gas law. Using the fact that the flow through the PFEIFFER valve only depends on the pressures  $P_i^{\text{tank}}$  and  $P_i^{\text{cell}}$ , assuming that  $P_1^{\text{tank}} = P_2^{\text{tank}}$  leads to

$$\begin{aligned} \dot{n}_2^{\text{mem}}(P_2) &= \dot{n}_1(P_2) - \dot{n}_2^{\text{cell}}(P_2) \\ &= \frac{V_1}{RT_1} \cdot \dot{P}_1(P_2) - \frac{V_2}{RT_2} \cdot \dot{P}_2(P_2) \end{aligned} \quad (3.11)$$

Figure 3.11(a) shows the computation steps visually using the respective plots versus time.

As the temperature of the system is regulated ( $T = T_1 = T_2 = \text{const.}$ ) and because  $V = V_1 \approx V_2$  since  $V_{\text{mem}} \ll V_1$ , equation eq. (3.11) yields

$$n_2^{\text{membrane}} = \frac{V}{RT} \int_0^{t_2} (\dot{P}_1(t'_1) - \dot{P}_2(t'_2)) dt'_2,$$

with  $t'_1$  such that

$$P_1(t'_1) = P_2(t'_2).$$

Important at this point is the dependency of  $\dot{P}_1(t_1)$  on  $t_1$  while the integration is over  $t_2$ .

As the experimental setup yields discrete values at given time intervals  $\Delta t$ , the data evaluation makes use of a sum rather than an integration.

$$n = \frac{V}{RT} \sum (\dot{P}_1(P_1 = P_2) - \dot{P}_2(P_2)) \cdot \Delta t \quad (3.12)$$

yields the molar amount of hexane condensed inside the membrane. Figure fig. 3.11(b) shows the result of the integration eq. (3.12) for membrane 296d. It is an absorption and desorption isotherm for hexane inside the porous alumina membrane. The bulk condensation and evaporation is not visible, as it is also recorded with the reference isotherm without membrane inside the cell.

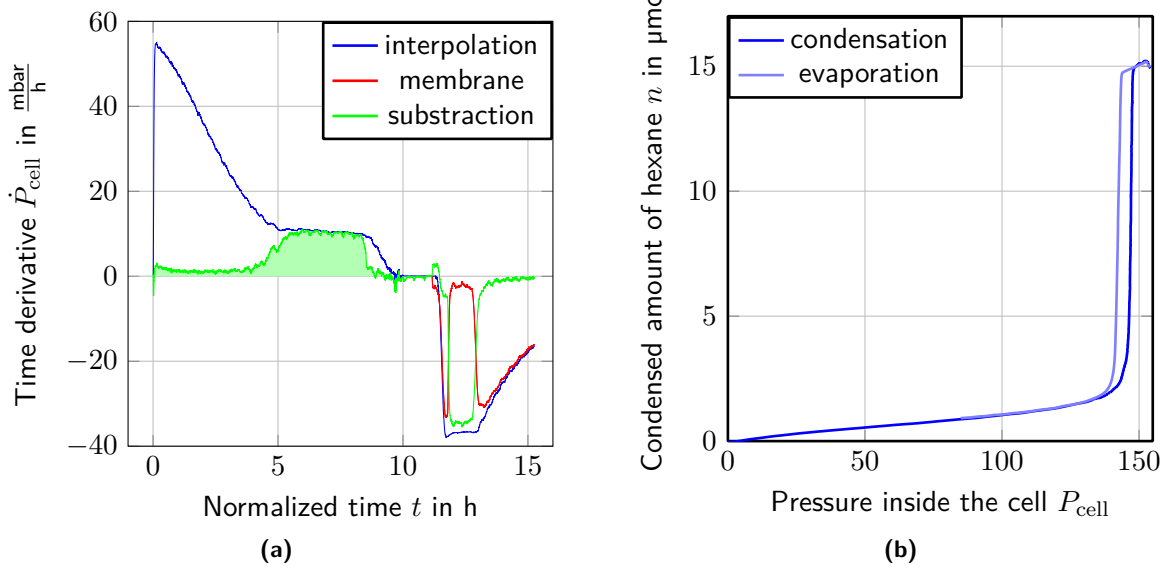


**Figure 3.11** (a) shows the raw data of the isotherm with membrane and interpolation of the reference isotherm without membrane. Also, the subtraction of the latter (compare integrand of eq. (3.11)) is plotted where the area to be integrated for the absorption and desorption isotherm is shaded light green. The integration according to eq. (3.12) results in the isotherm displayed in (b).

What strikes the eye is the sharp rise of the condensation branch that does not start at the liquid fraction  $LF = 0$ . The same goes for the evaporation branch. It only drops to a liquid fraction value  $LF > 0$  and then decreases superimposed with the condensation branch. The reason for this initial rise of the isotherms could be due to the build up of a film on the membranes surfaces due to the attraction by the pores' walls. This is part of the theory of condensation and evaporation in confinement even though the film is ignored in the basic KELVIN equation (section 2.2).

The pressure inside the cell  $P_{\text{cell}}$  can be translated to pore diameters  $d_{\text{pore}}^{\text{Kelvin}}$  using the KELVIN equations eq. (2.2) and eq. (2.3). As this computation is just a model that needs to be tested for small pore diameters, oftentimes the isotherms are plotted on a relative pressure

$$P_{\text{rel}} = \frac{P_v}{P_{\text{sv}}}.$$

Furthermore, to simplify the comparison of isotherms measured for different membranes, the condensed amount of hexane  $n$  is converted to the liquid fraction  $LF$  by deviding by the maximum value of  $n$  for most of the displayed isotherms.

For the computation of the introduced physical sizes, the saturated vapor pressure  $P_{\text{sv}}$  must be determined.

### 3.5.1.1 Porosity

As explained in section 3.2, knowing the porosity of the membranes allows to do a more precise analysis of the SEM images. To this end, the porosity of the membranes is computed from the molar amount of matter of hexane condensed within the membranes' pores (eq. (3.12)). Furthermore, for the pressure range 0 mbar to 160 mbar, hexane in its liquid form can be regarded as incompressible and therefore the hexane's volume be computed via

$$V_{\text{hex}} = n_{\text{hex}} \cdot V_{\text{mol,hex}}.$$

. The thickness  $l_{\text{pore}}$  of the membranes is determined by SEM images. This works sufficiently precise since the magnitude of the membranes' thickness is micrometers and the contrast between the carbon

tape and the membrane itself is very sharp. Finally, the area  $A_{\text{membrane}}$  of the measured membranes is derived from a binocular image.

Using these photophoto information, the porosity  $\phi$  of a given membrane is

$$\phi = 1 - \frac{V_{\text{hex}}}{V_{\text{mem}}},$$

with the membrane's volume

$$V_{\text{mem}} = A_{\text{mem}} \cdot l_{\text{pore}}.$$

### **3.5.1.2 Determination of the saturated vapor pressure**

As the bulk condensation plateau shows a slight drift (compare figure fig. 3.10), using the maximum measured pressure  $P_{\text{cell}}$  does not yield the saturated vapor pressure  $P_{\text{sv}}$  but a higher value. In addition, depending on the contamination of the system by air or degassing grease, the measured value for  $P_{\text{sv}}$  shifts due to the partial pressures. To probe the reproducibility of an isotherm loop including the grade of contamination, the maximum measured pressure for different membranes is compared. As the system is opened to replace the membrane in between the isotherms, each cycle is independent. For the change of membrane process please read section 3.4.1.1. The result of the experiment is that  $P_{\text{sv}}^{\text{exp}}$  fluctuates by

$$\delta P_{\text{sv}}^{\text{exp}} = \pm 0,5 \text{ mbar}.$$

To compute the isotherms from the recorded data the experiment needs to be conducted not only with a membrane inside of the cell, but also with an empty cell. As the relevant plateau of condensation and evaporation inside the pores of the membrane occur at about

$$P_{\text{plateaus}} = 140 \text{ mbar},$$

$\delta P_{\text{sv}}^{\text{exp}}$  translates to an error of about

$$\delta P_{\text{rel}} \leq \pm 0,005.$$

#### ADD DIAMETER ERROR

Moreover, there might be a temperature gradient within the cell. It is not clear that the membrane's temperature is the same as the temperature measured on the copper clamp. The condensation and evaporation processes inside the cell heating and cooling the membrane respectively can cause its temperature to be different from the copper clamp's. ADD ERROR COMPUTATION???

### **3.5.1.3 Diameter error using Kelvin equation**

GAUSSIAN error propagation to check the precision of the experiment.

### **3.5.2 Optical measurements**

As mentioned in section 3.3, the light transmission setup is independent from the volumetric measurements and also the evaluations do not depend on each other. The light transmission is rather a tool to check on the theory of evaporation and condensation within the membrane using a different approach.

To compute the transmission coefficient of a membrane, it is measured in dry state yielding  $T_{\text{mem}}^{\text{dry}}$ . In contrast to the transmission measurements during an isotherm where the membrane is placed within the cell behind sapphire windows, the dry transmission measurement is done without the cell.

Therefore, the following computation yields a transmission coefficient that needs to be corrected by the windows' transmission. It is the transmission drops upon condensation and evaporation that are of interest though. And since they show magnitudes of  $10^{-4}$ , the correction is neglectable. Finally, the first measured intensity value  $I_0$  of a given isotherm is assigned to the dry coefficient as at this point, no hexane is condensed inside of the membranes pores yet (the system has just been pumped). From there on, each intensity measurement is translated to a transmission coefficient according to

$$T(t) = T_{\text{mem}}^{\text{dry}} \cdot \frac{I_0}{I(t)}. \quad (3.13)$$

At this point it must be mentioned, that the conducted transmission measurements showed quite large variations even on a single membrane. Upon shifting the membrane respectively to the laser beam, for one membrane the transmission could be varied by 50 %. While the mentioned membrane was an exception regarding these uncertainties, tilting the membrane also caused the transmission to vary. For better results, all membranes have been measured twice. In between the two measurements, the membranes were removed from the setup and then positioned with the other surface facing the HeNe laser.

## 4 Experimental results

### 4.1 Experimental approach

For the first time during the team's research on alumina membranes, systematic measurements were conducted. Due to the limited period of time, only some aspects of the membranes could be investigated in more detail. During the internship, I measured 25 membranes of 3 wafers using the experimental setup described in section 3.3. Table 4.1 summarizes the main features of these wafers.

Victor Doebele's initial measurements previous to this internship had already shown strong dispersions in the properties of the membranes of different wafers, but also within the same wafer. Therefore, my goal was to perform systematic measurements on alumina membranes to determine the source of these dispersions. To probe a possible dependency on the position of the membranes on the wafers, the labeling is done according to the convention shown in fig. 4.1.

Due to the limited period of time, I chose to focus on the production step of the *barrier layer* dissolution (compare section 3.1.3) and the pore diameter reduction by atomic layer deposition. During the internship, I measured 25 membranes of 4 wafers using the experimental setup described in section 3.3. Table 4.1 summarizes the main characteristics of these wafers. A processing scheme for the wafers 295 and 296, which also marks the conducted measurements, is given by fig. 4.2.

### 4.2 Membrane structure analysis

#### 4.2.1 Isotherm of an open pore membrane

Section 4.2.1 shows a typical isotherm obtained from the measurements of an open pore membrane (in this case membrane 296b'). The dependence of the liquid fraction  $LF$  on the relative vapor pressure  $P_{\text{rel}}$  follows the behaviour expected for a porous material: The membrane fills at a pressure

$$P_{\text{cond}}^{296b'} < P_{\text{sv}}$$

and empties at an even lower pressure

$$P_{\text{evap}}^{296b'} < P_{\text{cond}}^{296b'} < P_{\text{sv}},$$

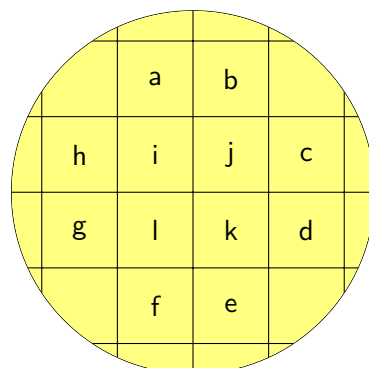


**Figure 4.1** Convention used to assign membrane depending on their position on the wafer.

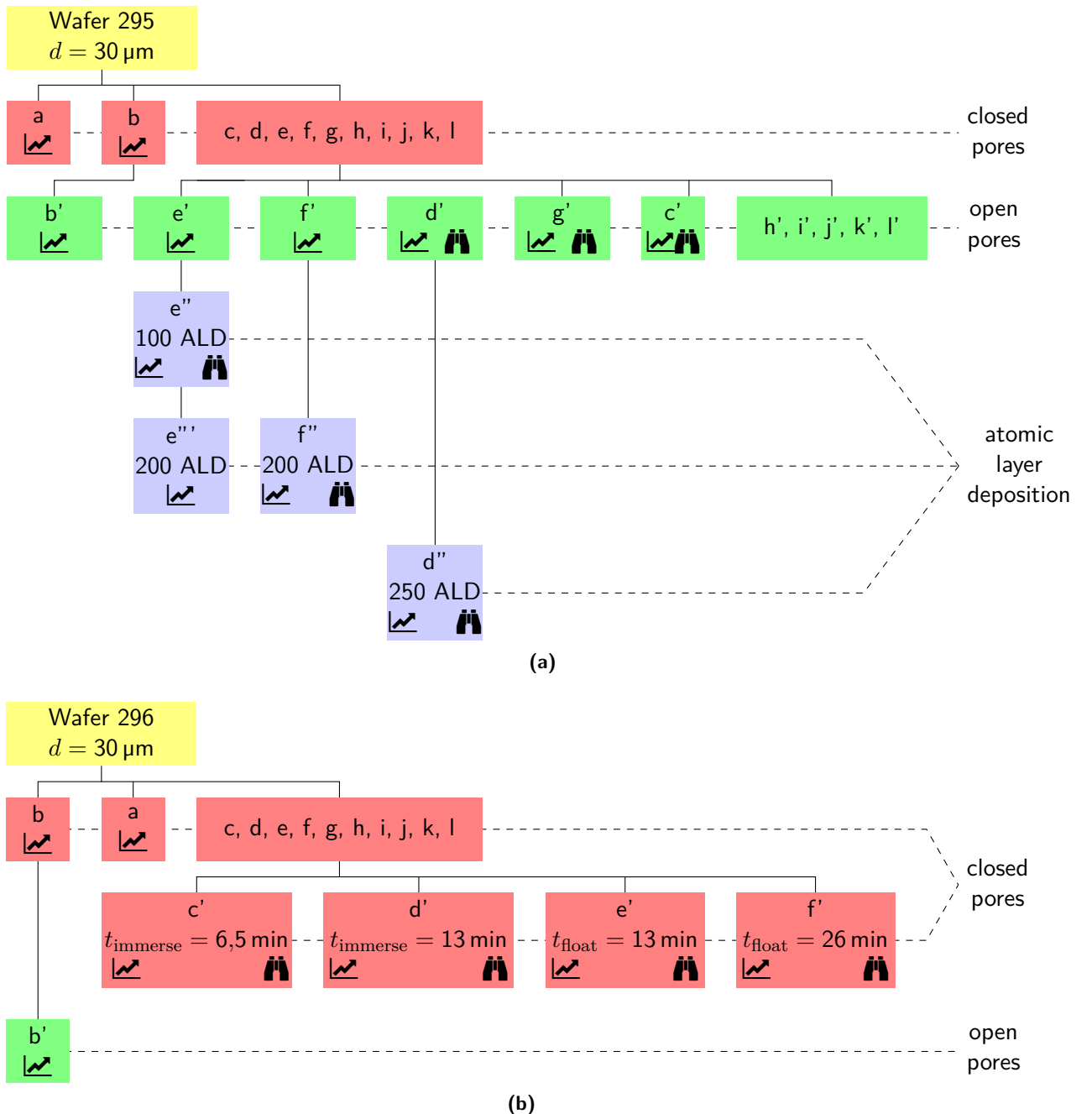


**Figure 4.2** Wafer 295 and 296 processing scheme. While a signifies a recorded isotherm, the means MEB pictures have been taken. Red marks pores closed on one end, green pores open on both ends. The processed wafers are immersed in phosphoric acid for  $t_{immerse}$  or floated on for  $t_{float}$ .

**Table 4.1** Wafer specifications. The wafers thickness  $l_{\text{pore}}$ , floating time  $t_{\text{float}}$  of the *barrier layer* dissolution process and pore diameter dispersion  $\Delta d_{\text{pore}}^{\text{MEB}}$  measured by electron beam microscopy are noted. The latter two parameters apply to the open pore membranes of the respective wafer.

Wafer	$l_{\text{pore}}$ [μm]	$t_{\text{float}}$ [min]	$\Delta d_{\text{pore}}^{\text{MEB}}$ [nm]
292	60	36+4	-
294	60	33	-
295	30	35 (38 for b)	7
296	60	40	-

hereby displaying a hysteretic cycle. By the model of condensation and evaporation in an open pore, which was introduced in section 2.3, a condensation at spinodal pressure  $P_{\text{sp}}$  and evaporation at equilibrium pressure  $P_{\text{eq}}$ , with

$$P_{\text{eq}} < P_{\text{sp}} < P_{\text{sv}},$$

are expected. This is coherent with the observations as the shape of the volumetric isotherm qualitatively matches the theoretical loop displayed in fig. 2.6(b).

For the transmission measurement, two drops corresponding to the condensation and the evaporation are observed, as expected according to section 2.5. Moreover, higher transmission is observed for the filled state of the membrane than for the empty state. This is also coherent with the theory of index matching mentioned in section 2.5.

The dashed lines in section 4.2.1 mark the average condensation and evaporation pressures of the isotherm. For their determination, the steepest point of the liquid fraction graph is sought, which corresponds to the minima of the transmission signals as expected. Converting these to diameters using the KELVIN equations eq. (2.3) and eq. (2.2) yields

$$\begin{aligned} d_{\text{pore}}^{296b'}(P_{\text{rel,sp}}^{296b'} = 0,956) &= 44,4 \text{ nm}, \\ d_{\text{pore}}^{296b'}(P_{\text{rel,eq}}^{296b'} = 0,925) &= 51,3 \text{ nm}, \end{aligned}$$

which makes for results within the range of expected pore diameters. Furthermore, the transmission behaves according to theory in regard of the filled transmission in filled state being stronger than for the empty state. (COMPARE TO SEM OF 296e????)

However, if all the pores were cylindrical, the condensation and evaporation branches would be expected to be vertical. The inclination of evaporation branch could result from funnelization of the pores as has been explained in section 2.3.4. The SEM images of the membranes support the assumption of funnelled pores as different pore diameters are observed for the top and bottom side (please refer to fig. 4.4 for an example). The condensation at spinodal pressure should still be vertical for weak funnelled pores, though. On the other hand, condensation at spinodal pressure in weakly funnelled cylindrical pores (compare section 2.3.4). This leads to the conclusion, that the pores are not only funnelled, but also distributed in diameter.

#### 4.2.2 Isotherm of a closed pore membrane

Section 4.2.2 shows the isotherm obtained on the same membrane 296b, but prior to the *barrier layer* dissolution step. The open pore membrane's isotherm is also displayed for the sake of comparison. The results show that the hysteresis cycle is much smaller for closed pores than it has been observed for open pores. In detail, the condensation branch is shifted to much lower pressures, while the evaporation branch shows only a slight shift in the same direction.

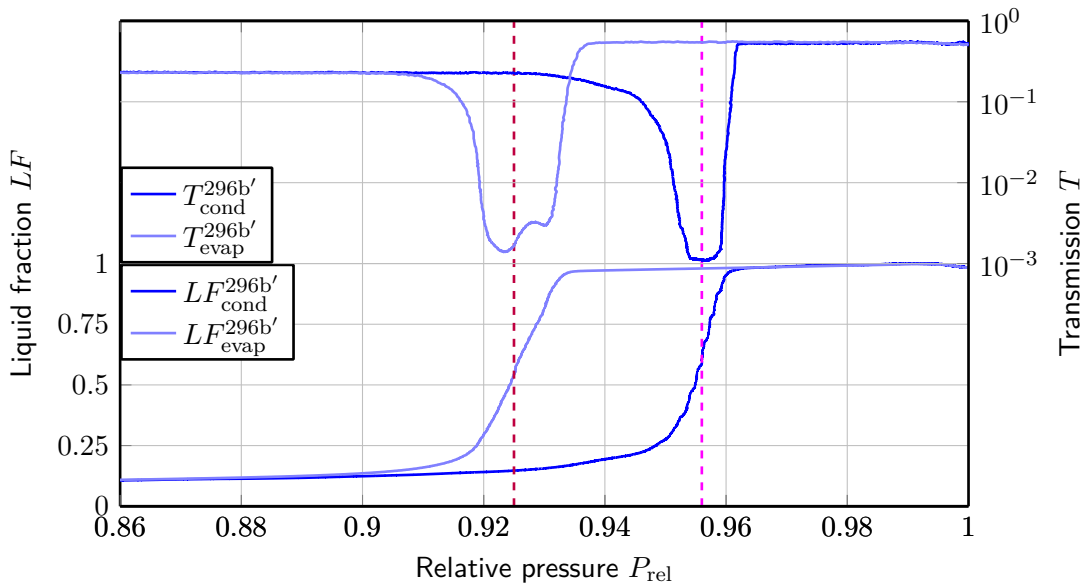


**Figure 4.3** Measurement results of open pore membrane 296b'. The dashed lines mark the average condensation and evaporation pressures.

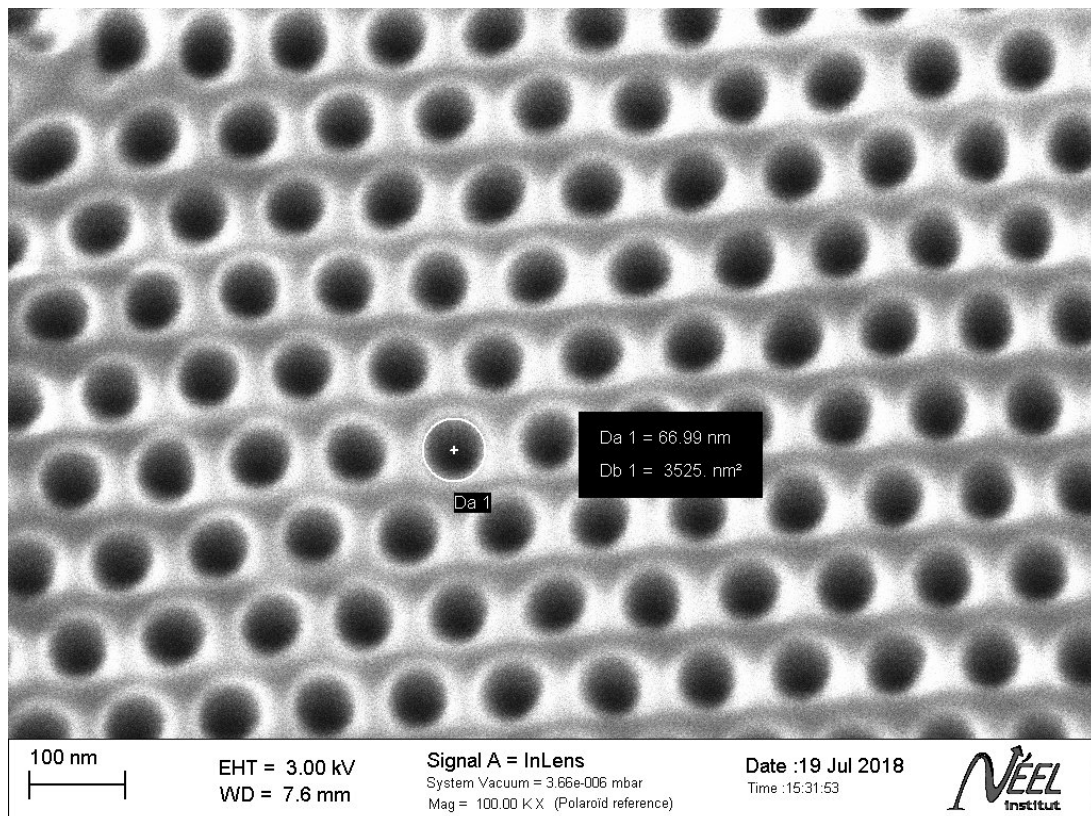
As will be explained in section 4.3, a small shift to lower pressures for the closed pore membrane is expected due to the widening of the pores during the *barrier layer* dissolution process. Since, according to section 2.3.2, the condensation occurs at equilibrium pressure in a closed pore, the smaller hysteresis of membrane 296b in comparison to 296b' is expected. However, as displayed in fig. 2.6(a), the volumetric isotherm of a closed pore membrane should not show a hysteresis at all, not for straight pores and neither for funnelled pores. Its presence can be explained by variations of the pore diameters along the pores' lengths. These variations are so called *corrugations*. The phenomenon of the hysteresis appearing for closed pores has been observed and accounted to corrugations by various experimentators (REF???).

As for the transmission, the drops correspond to the condensation and evaporation branch and also the effect of index matching is observed as expected from section 2.5. What remains to be understood is the extreme difference in magnitude between the transmission drops of the closed pore and the open pore membrane. In this magnitude, the phenomenon has only been observed for this specific membrane 296b so it might also be due to a light source within the experimental room that has not been turned off. As the membrane has been further processed, the measurement cannot be repeated though.

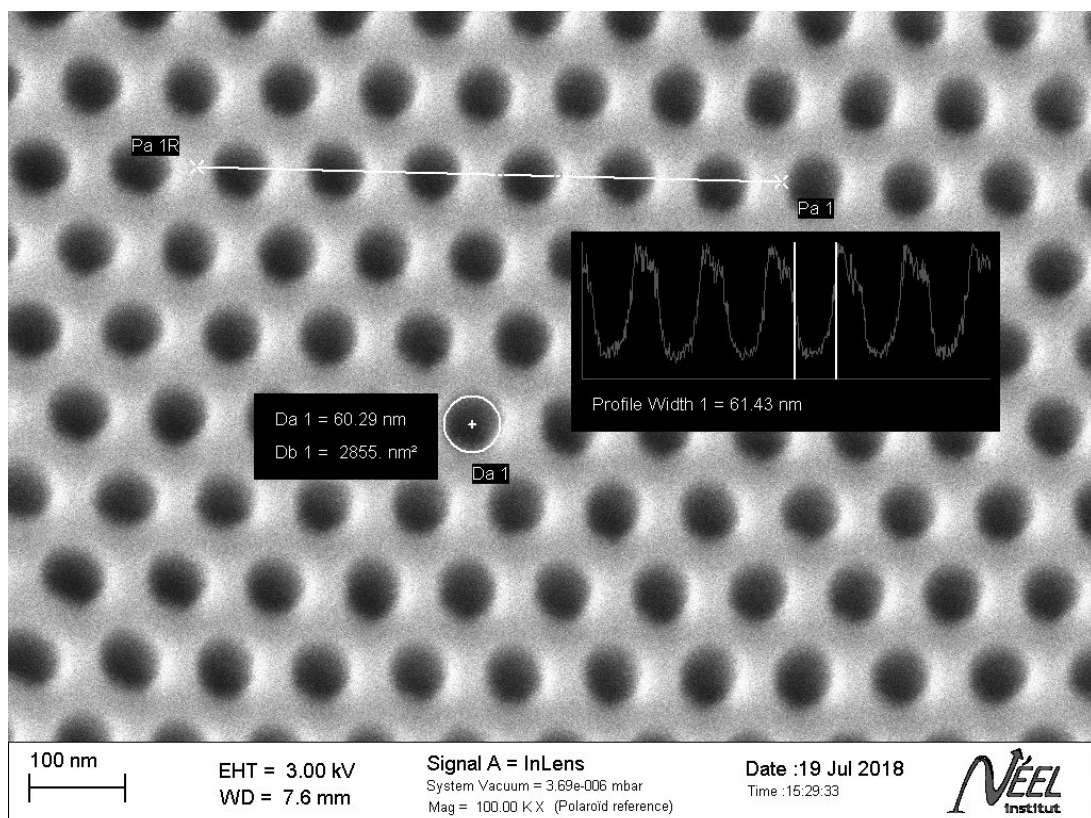
### 4.2.3 Measurement reproducibility

To check the reproducibility of the isotherm measurements, membranes were measured several times. Section 4.2.3 shows four consecutive measurements for the same open pore membrane 292c and one more independent measurement ( $LF_{\text{cond/evap}}^{292c,5}$ ). The biggest experiment deviation is the liquid fraction before the sharp rise of the condensation branch. However, this does not affect the position of the condensation and the evaporation rises, which are used to determine the pores' diameters.

As at the time of these experiments the laser transmission setup had not been in place and later membranes were measured only two times at maximum, the reproducibility of the laser transmission measurements cannot be assessed here.



(a)



(b)

**Figure 4.4** SEM images of membrane 295g' implying the pores' funnelling. The pores on the solution side (a) show bigger diameters than those on the aluminum side (b).

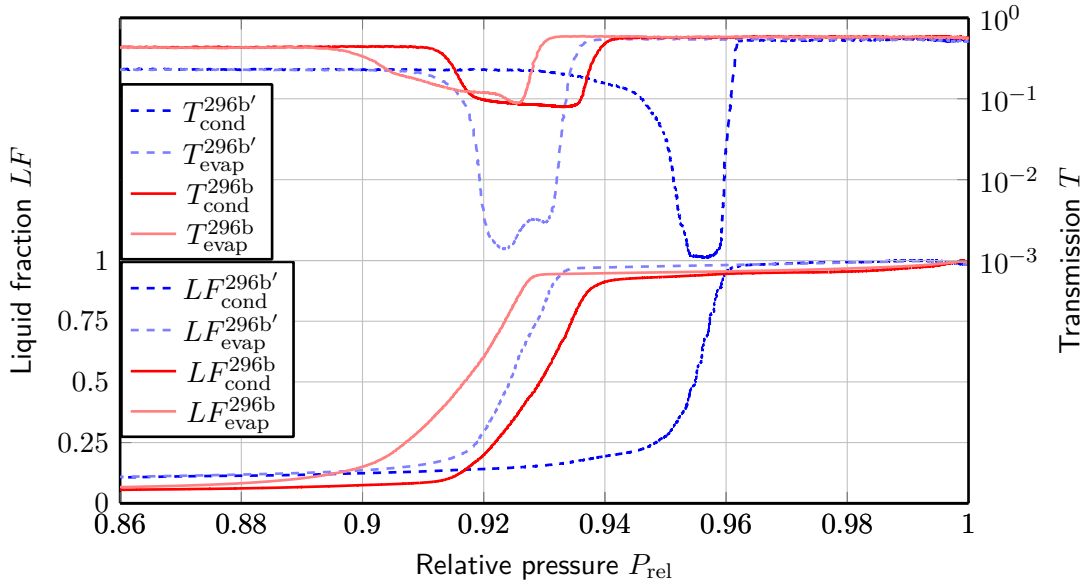


**Figure 4.5** Measurement results of closed pore membrane 296b in comparison to the open pore membrane 296b'.

#### 4.2.4 Inhomogeneities on one wafer

In this section, the isotherm measurements I performed in order to test the homogeneity of the wafers are presented for two production steps: The closed pore state after the aluminum dissolution process (compare section 3.1.2) in fig. 4.7 and the open pores after the *barrier layer* dissolution (section 3.1.3) in fig. 4.8.

For both wafers the overall shapes of the different membranes' isotherm measurements matches. The only exception is the open pore membrane 295c', which will be discussed in ??. However, the results show that there is a dispersion on the condensation and evaporation branches. This implies a dispersion on the pore size distribution of about

$$\begin{aligned}\Delta d_{\text{closed-pore}}^{296} &= 3,5 \text{ nm} \\ \Delta d_{\text{closed-pore}}^{295} &= 4,7 \text{ nm}\end{aligned}$$

for the closed pore membranes and

$$\begin{aligned}\Delta d_{\text{open-pore}}^{292} &= 4,1 \text{ nm} \\ \Delta d_{\text{open-pore}}^{295} &= 3,5 \text{ nm}\end{aligned}$$

for the open pore membranes. The computations were done using the pressures of the top end of the widest spread evaporation branches of the respective wafer

$$\begin{aligned}P_{\text{evap,top}}^{296b} &= 0,9275, & P_{\text{evap,top}}^{296e'} &= 0,9225, \\ P_{\text{evap,top}}^{295a} &= 0,9375, & P_{\text{evap,top}}^{295b} &= 0,9325, \\ P_{\text{evap,top}}^{292c} &= 0,9275, & P_{\text{evap,top}}^{292d} &= 0,9325, \\ P_{\text{evap,top}}^{295d'} &= 0,9430, & P_{\text{evap,top}}^{295e'} &= 0,9400,\end{aligned}$$

as these correspond to the emptying of the largest pores of a given membrane.

Moreover, the transmission during the condensation and the evaporation of hexane within the membranes also shows dispersions across the wafers. Figure 4.9 shows color maps of the dry transmission of the membranes of the wafers 295 and 296. The membranes of wafer 296 have all been measured before any further treatments with phosphoric acid, whereas the membranes of wafer 295 are open

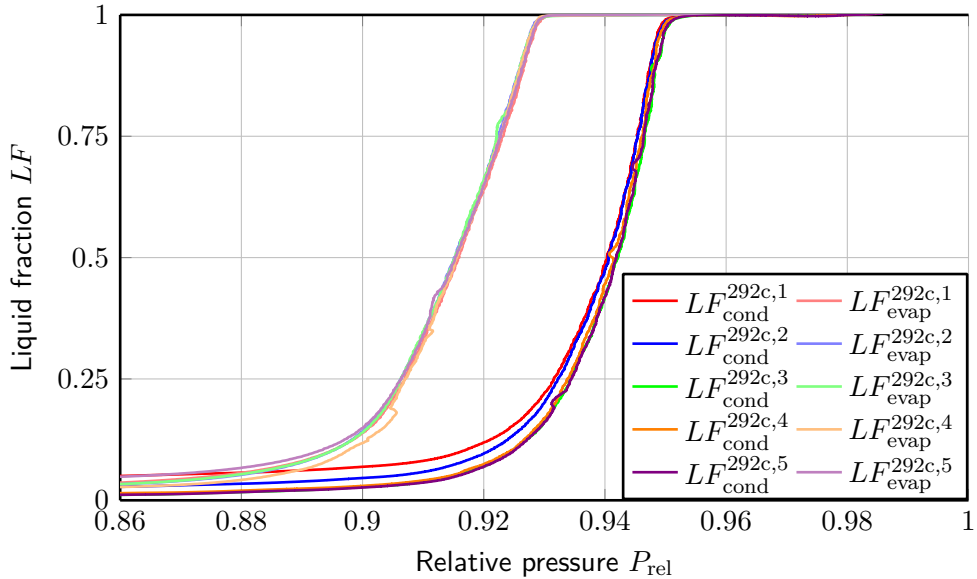


**Figure 4.6** Reproducibility test comparing multiple isotherms measured for the same membrane 292c.

pore membranes except for 295a and 295b, which are still closed. In comparison to the theoretical values computed using the FRESNEL equations (compare eq. (2.7)), the measured transmission coefficients are much smaller. This can be explained by the pores scattering light as explained in section 2.5. Talking wafer inhomogeneities, the measured transmission of membranes on the same wafer shows variations of up to 8 % for the closed pore membrane of wafer 296 and 17 % for the open pore membranes of 295. A systematics regarding the link between the pore diameters and the transmission value can be suspected when regarding the membranes 296a, 296b, 296e and 296f. For each pair of two neighboring membranes, the same transmission has been measured. The respective isotherms are displayed in fig. 4.7(a). What strikes the eye is that the neighboring pores show almost perfectly superimposed volumetric isotherms, whereas there is a clear shift in pressure between the two pairs' curves. To draw a conclusion, larger pore diameters (higher condensation pressures) go together with a stronger dry transmission. This conclusion has to be retested using other membranes as it has only been observed once.

In conclusion, to measure the effect of treatments on a given membrane, before and after measurements are necessary. It is not enough to measure one membrane representatively for multiple membranes in the same state.

#### 4.2.4.1 Transmission of open and closed pores

Figure 4.9(b) shows the measured dry transmission for the membranes of wafer 295. The membranes 295a and 295b are still closed pore membranes, while all other membranes have undergone the *barrier layer* dissolution process opening their pores. Striking is the much better transmission of the closed pore membranes in comparison to the open pore membranes. Referring to the assumption made in section 4.2.4, that larger pores cause stronger light scattering and therefore weaker transmission, the observed phenomenon could be explained by the increase of pore diameters upon the pore opening step. To verify this explanation, systematic experiments using the same open pore membrane and widening the pores by immersion in acid could be conducted.

#### 4.2.5 Defects

All in all, the conducted measurements yield great results. The measured isotherms go along with the model introduced in section 2.3 and are reproducible. The inhomogeneity on a given wafer is

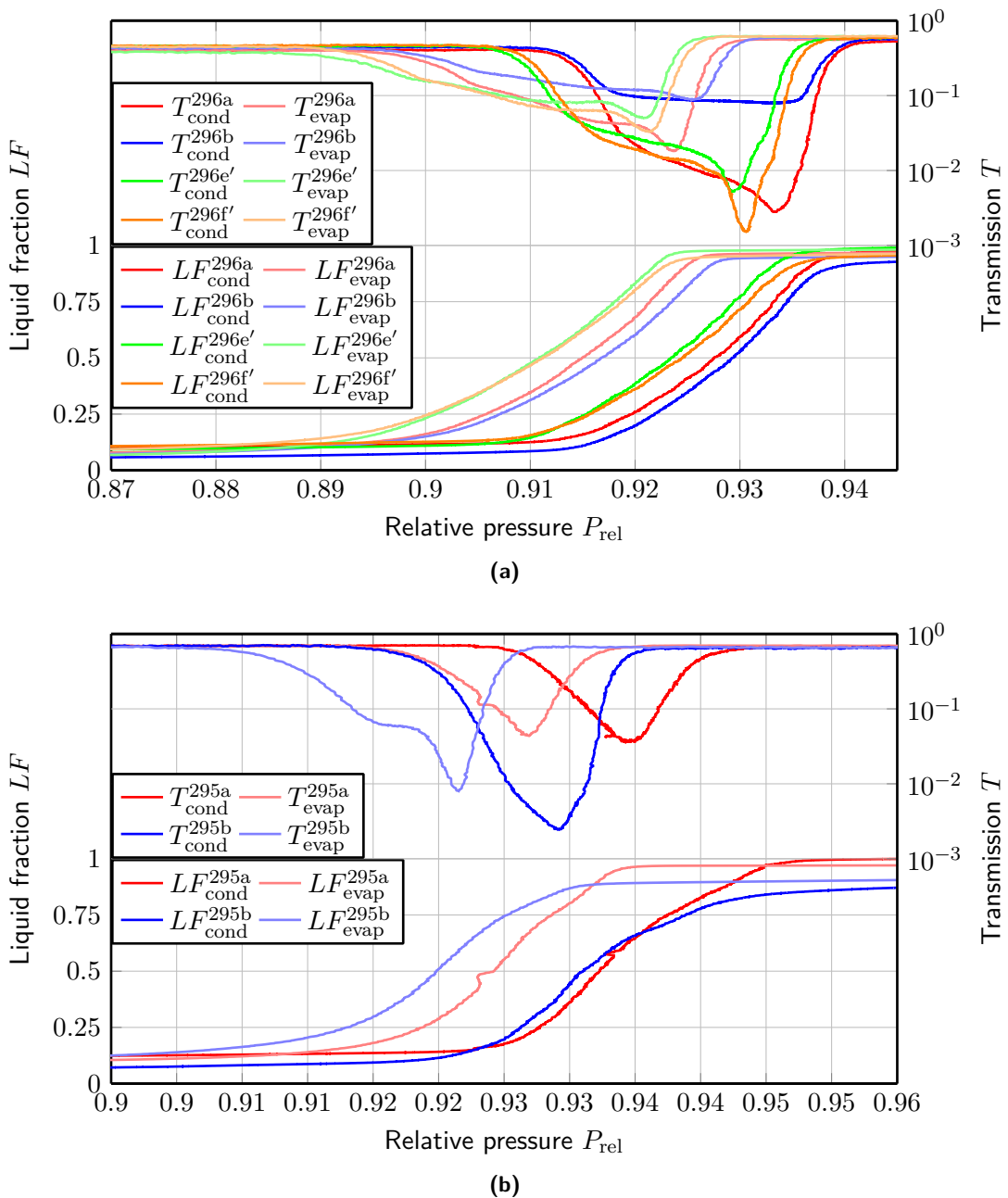


**Figure 4.7** Comparison of closed pore membranes of one wafer. (a) compares membranes of wafer 296 while fig. 4.7(b) deals with 295.

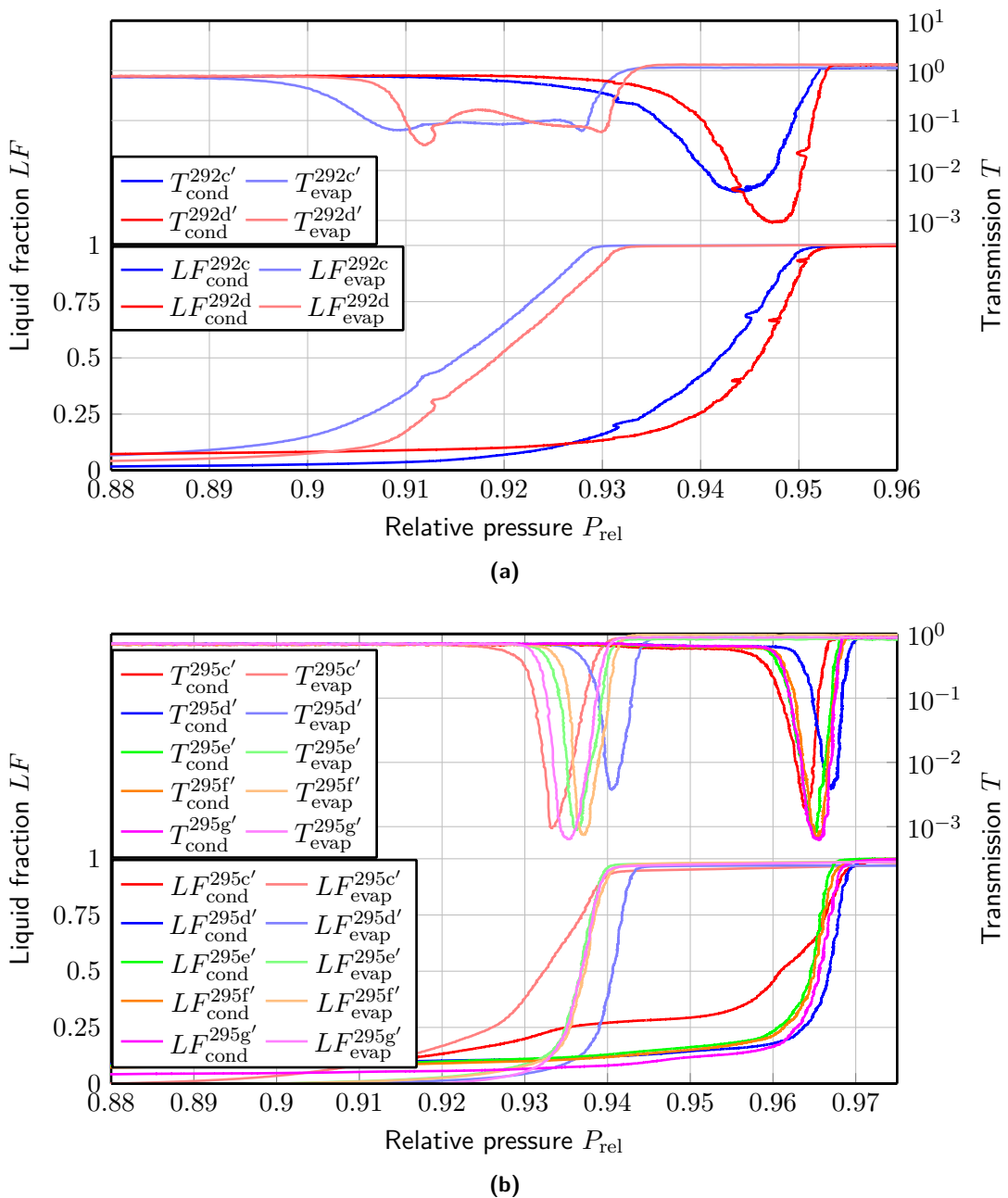
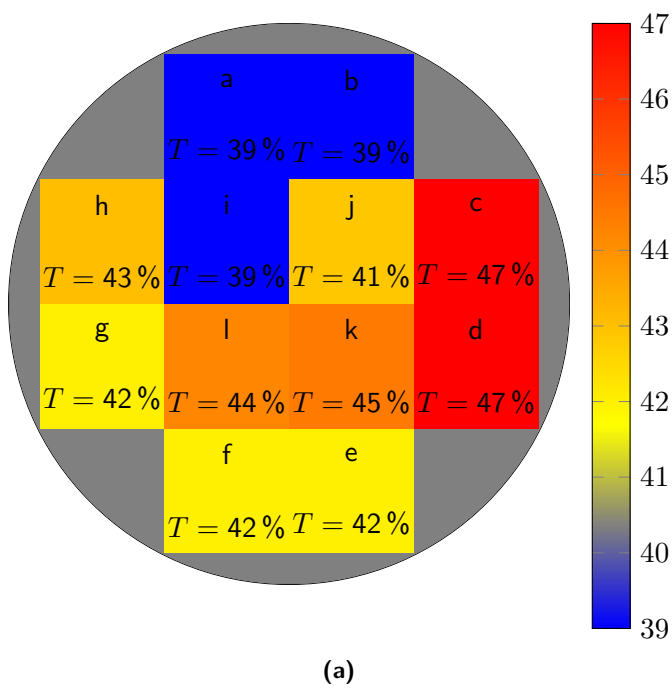
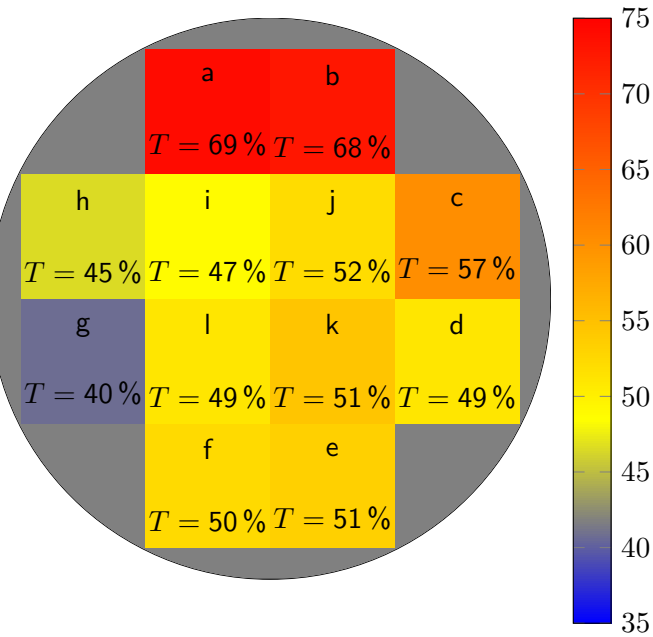


**Figure 4.8** Comparison of open pore membranes of one wafer. (a) compares membranes of wafer 292 while fig. 4.8(b) deals with 295.



(a)



(b)

**Figure 4.9** Transmission measurements of wafer 296 (a) and wafer 295 (b). Wafer 296 has been measured in untreated closed pore state. The membranes 295a and 295b are closed pore membranes while the rest of wafer 295 has been opened.

bearable???

Nevertheless, pore defects and dispersions were detected. First, there is the pore size distribution. To estimate its broadness, SEM images are analyzed in 295g???. Next, the funnellization and the corrugation must be mentioned. Both cause intra pore diameter variations that cause inclined isotherms, even for a single pore. Last, bad open pores were detected during the measurements. This problem will be discussed in the following section, as its examination leads to valuable, relevant results.

## 4.3 The problem of pore opening

### 4.3.1 Bad open pores

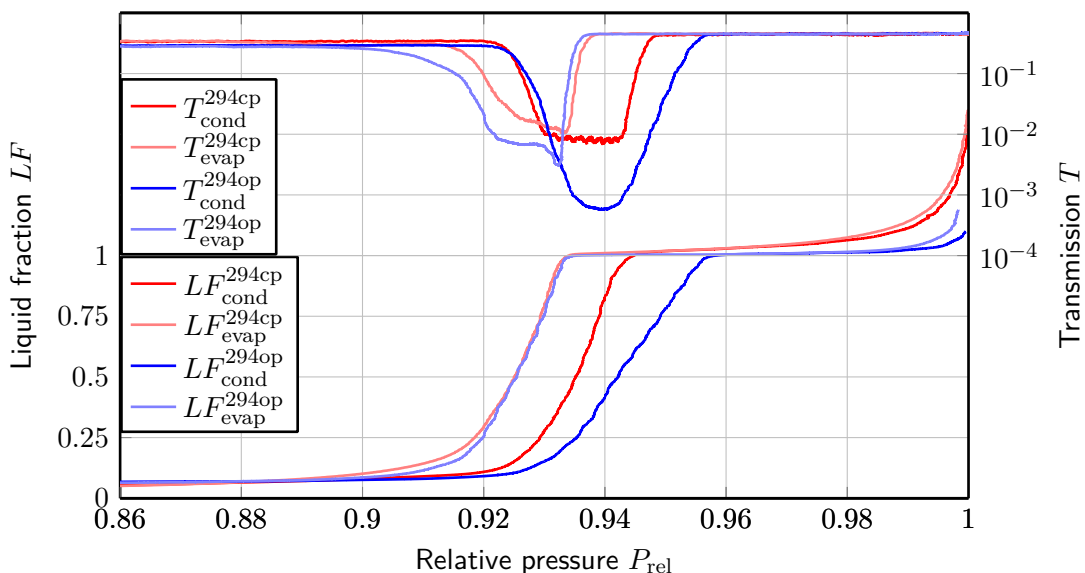
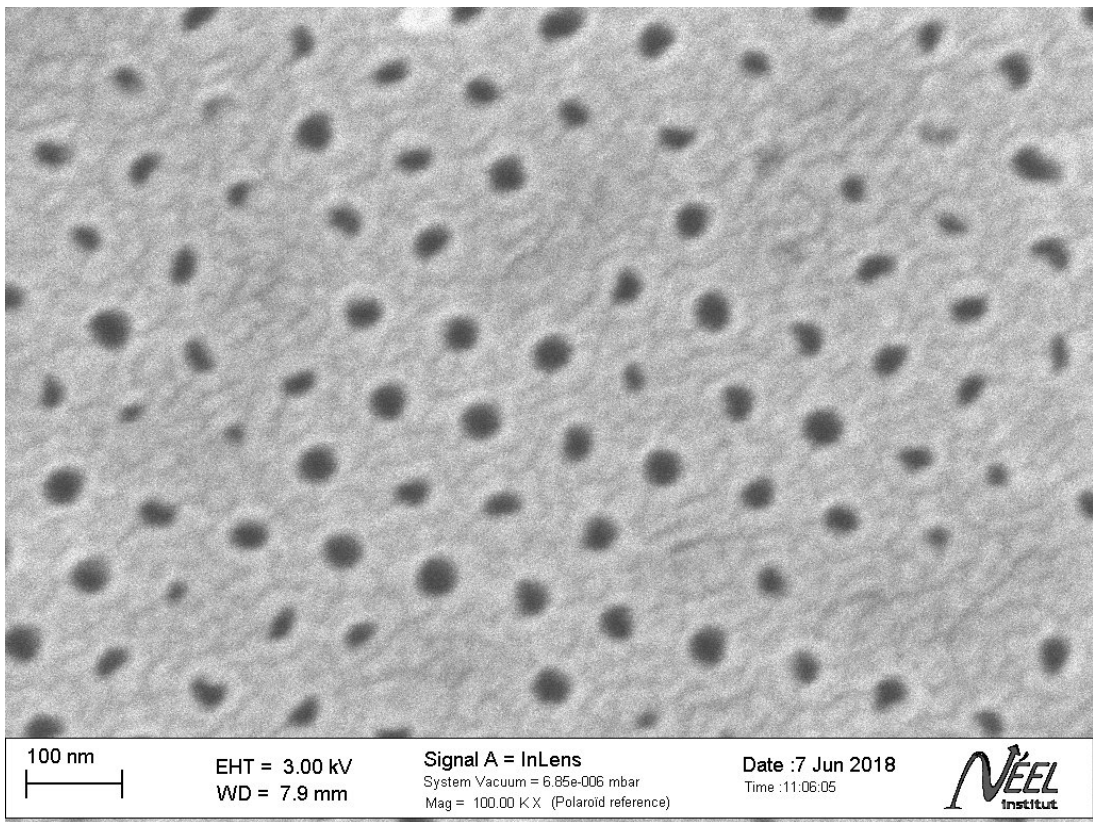


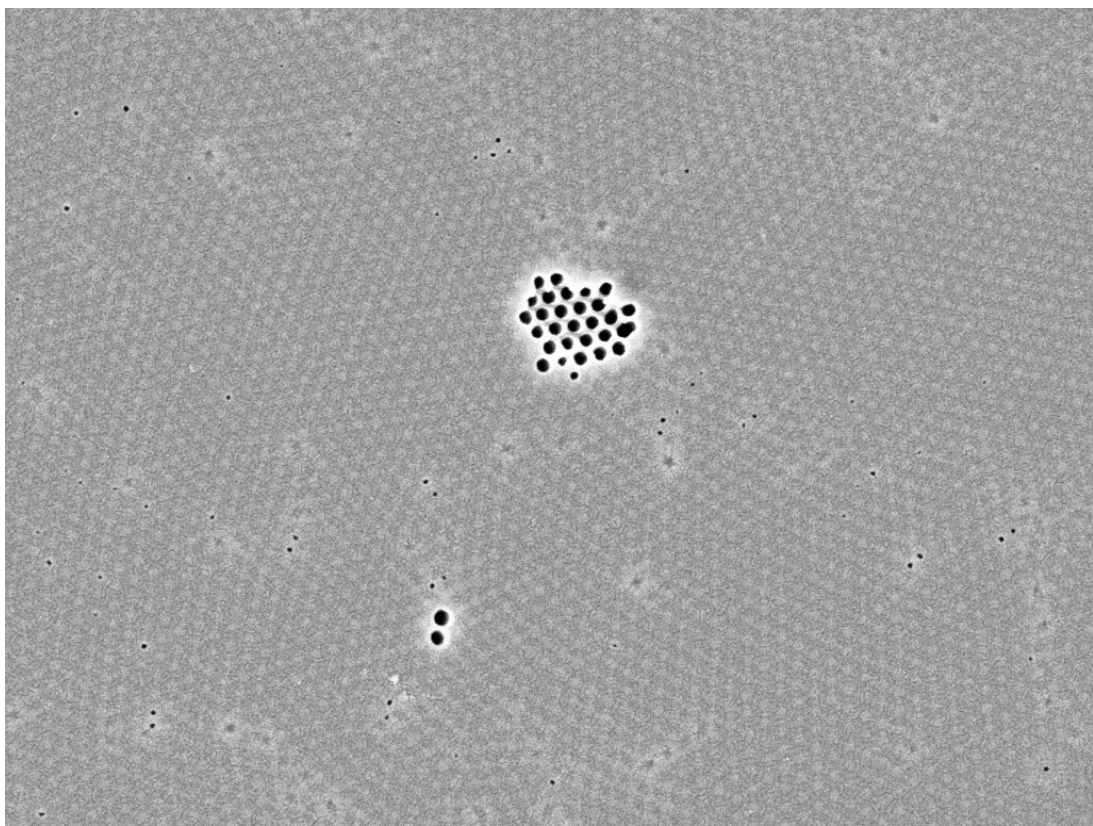
**Figure 4.10** Bad open pores illustrated by the comparison of a closed pore isotherm and a open pore isotherm of membrane 294a.

Victor Doebele's measurements before my internship had revealed that the *barrier layer* dissolution step failed to open all the pores of some membranes. The term *bad open pores* refers to a membrane that has been floated on phosphoric acid for not long enough to completely open the pores. ???TIKZ IMAGE??? As a result some pores remain closed whereas others have constricted openings and some are fully open. Section 4.3.1 shows the comparison of closed pore membrane 294cp and membrane 294op with bad open pores. The assumption is derived from the isotherm in the following way: By theory, the condensation branch should be shifted towards higher pressure for open pores in respect to closed pores. While this is the case for membrane 294op's end of the condensation rise, it still starts at the same pressure as the condensation of the closed pore membrane which by theory condenses at equilibrium pressure. Moreover, the evaporation of 294op is superimposed with the one of 294cp. While this is expected by theory, it rules out the possibility of an increase in funnellization or corrugation causing the broader condensation branch of the open pore membrane. The only possible explanation for the observed behaviour is a population of open pores alongside one of closed pores on the membrane. In this case some pores start filling at equilibrium pressure, wheras others fill at higher spinodal pressures depending on the size of the pore opening on the aluminum side. Independently, SEM images of the membrane confirm the assumption of bad open pores as shown in fig. 4.11(a).

At first glance, resolving the bad open pore issue seems as easy as simply increasing the membranes' floating time during the *barrier layer* dissolution. On second thought though, a problem comes up:



(a)



(b)

**Figure 4.11** (a) shows a SEM image confirming the bad open pores of membrane 294op. Image (b) SEM image of a membran floated on phosphoric acid until the appearance of milky aspects. It is coherent with the link of the milky aspect to pores of a wafer starting to open.

Figure 4.11(a) clearly states that some pores open before others. Therefore, these open pores are infiltrated by phosphoric acid which starts etching the pore from the inside increasing its diameter. This results in a broadening pore diameter distribution on the membrane caused by the *barrier layer* dissolution process.

As mentioned in ???MEMBRANE PRODUCTION, milky aspects occur at some point of the floating. Same as for spinodal condensation in the membranes, the filling of the opening pores with acid is assumed to cause light scattering and can therefore be linked to these milky aspects. Proof of this theory is the SEM image taken of a membrane that has been floated until the milky aspects appeared. Shown in fig. 4.11(b), the image confirms the semi open state of the membrane. As the milky aspects last for about

$$t_{\text{milky}} = 3 \text{ min}$$

and the etch rate of phosphoric acid on alumina is expected to be

$$e = 1 \frac{\text{nm}}{\text{s}},$$

the barrier layer dissolution process should cause an increase of the pore diameter dispersion of

$$\Delta d_{\text{pore}} = 6 \text{ nm}.$$

This is quite dramatic regarding that the pore diameter distribution of a closed pore limited to about 10 nm ??? PROOVE!. Therefore, this increase should be obvious on the comparison of the evaporation branches of a closed pore membrane with an equivalent open pore membrane. Using section 4.2.2 as an example does not confirm these expectations. On the contrary, the evaporation branch seems to become more sharp by opening the pores. This leads to the suspicion that the etch rates parallel to the pore axis  $e_{\parallel \text{pores}}$  and perpendicular to the axis  $e_{\perp \text{pores}}$  are different. With the idea of using a combination of floating and immersion in phosphoric acid for the *barrier layer* dissolution, an experiment to calibrate the etch rates has been conducted.

Membranes of wafer 296 were floated and immersed in phosphoric acid for

$$\begin{aligned} t_{\text{im}}^{296c'} &= 6,5 \text{ min}, \\ t_{\text{im}}^{296d'} &= 13 \text{ min}, \\ t_{\text{fl}}^{296e'} &= 13 \text{ min}, \\ t_{\text{fl}}^{296f'} &= 26 \text{ min}, \end{aligned}$$

where  $t_{\text{im}}^i$  are the immersion times and  $t_{\text{fl}}^i$  the floating times with  $i \in \{296c, 296d, 296e, 296f\}$ . Assuming that the acid etches the *barrier layer* at the same rate from within and outside the pores, these floating and immersion of the membranes 296c' and 296e' should yield the same reduction of the thickness, the same holds for the membranes 296d' and 296f'. At this point, the initial thickness of wafer 296 is assumed to be

$$d_{\text{barrier-layer}}^{296} = 30 \text{ nm}$$

thick, same as for wafer 292. To probe the etch rate  $e_{\parallel}$ , SEM images are taken for all membranes after the treatment in phosphoric acid. These images also serve to measure the pore diameters on the solution side and hereby to calculate  $e_{\perp}$ . In addition, the pore diameters are checked using isotherm measurements.

### 4.3.2 Etch rate on the barrier layer

Figure 4.13 shows the SEM images taken of the membranes 296c' and 296e' after immersing and floating respectively. During the SEM session, a lot of drift and charging had to be dealt with which makes for a bad resolution of the images. However, what strikes the eye is the large thickness of

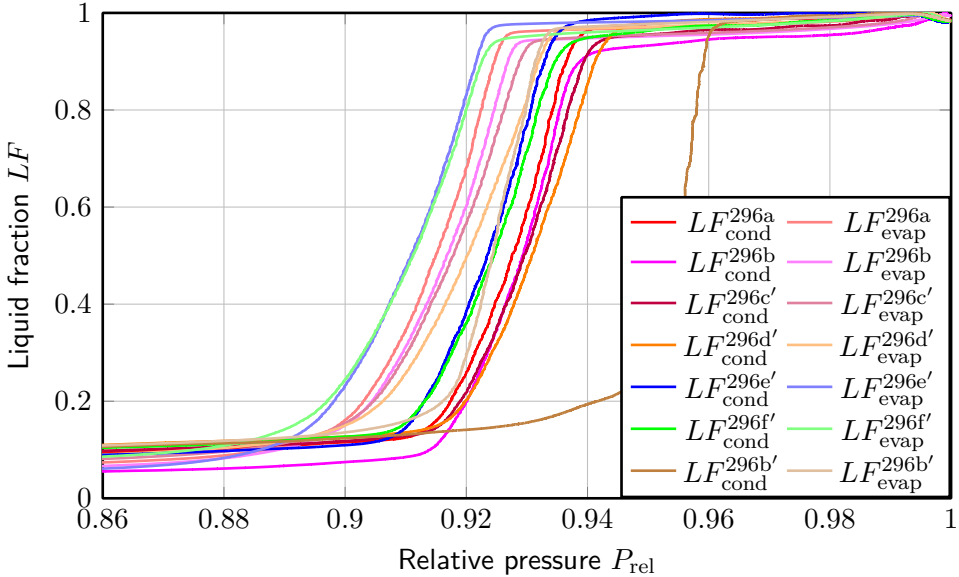


**Figure 4.12** Confirmation that the membranes 296c', 296d', 296e' and 296f' are still closed pore membranes after the treatments with phosphoric acid. The shapes of their isotherms match those of the untreated closed pore membranes 296a and 296b, whereas they do not show any shift of the condensation branch in direction of that of open pore membrane 296b'.

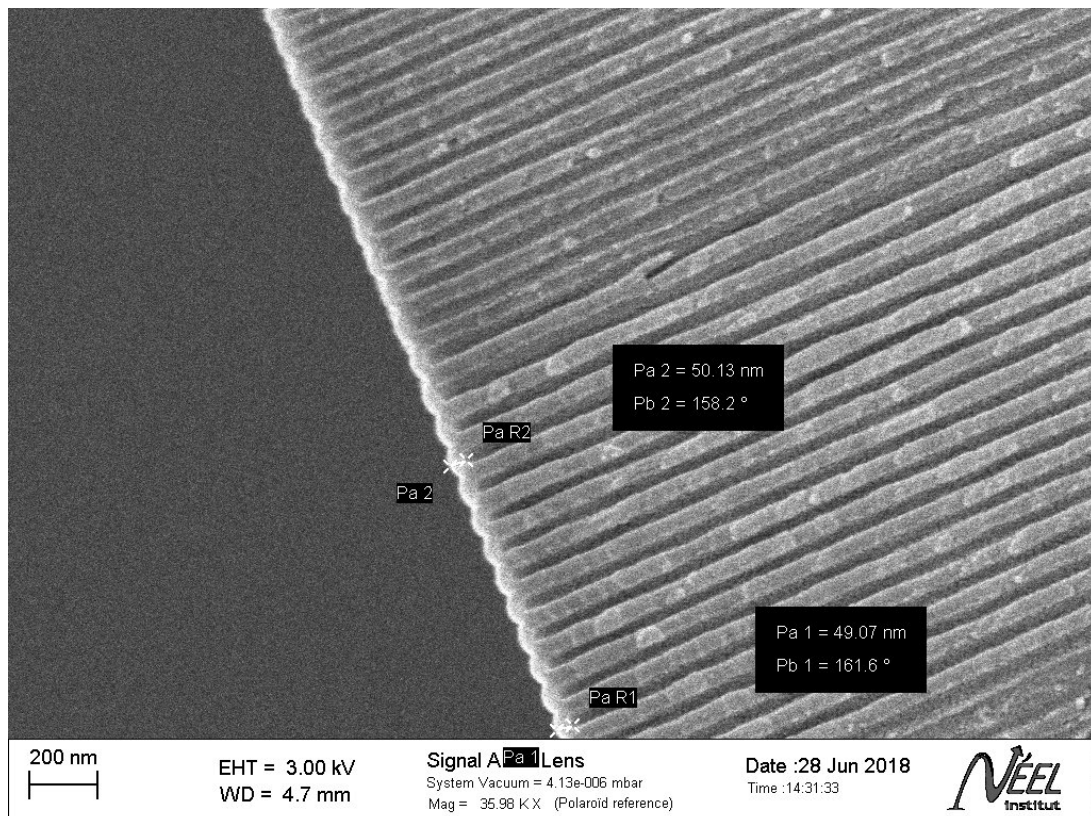
the *barrier layer*, even after the treatments with phosphoric acid, as it is still thicker than the initial thickness that has been assumed. In accordance with these SEM images, the isotherm comparison shown in fig. 4.12 implies pores that are still closed on all four treated membranes. In explanation, the isotherms superimpose nicely with the untreated closed pore membrane 296a and also, the direct comparison to the open pore membrane 296b' reveals a strong shift of the condensation branch towards lower pressures. Bad open pores can be excluded by comparing to section 4.3.1 and the corresponding explanations in section 4.3.1 (and from SEM images shown in appendix??)).

In conclusion, the anodization process (compare ???) does not yield the same *barrier layer* thickness for different wafers, even using the same parameters. To conclude with, SEM images of one native membrane that has not undergone any treatments with phosphoric acid needs to be measured to get an idea of the initial *barrier layer* thickness. If there are also dispersions of this thickness on one wafer remains to be probed.

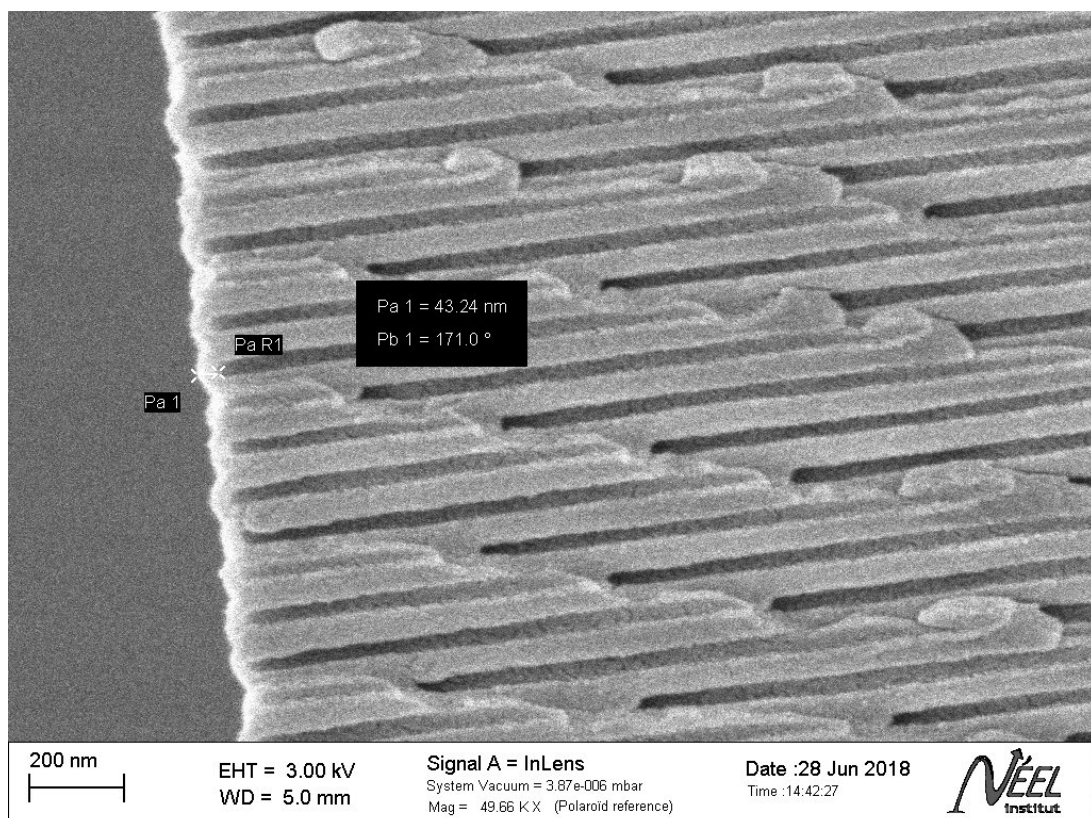
### 4.3.3 Increase of funnelling upon immersion in phosphoric acid

The comparison of the immersed membranes 296c' and 296d' with the native membrane 296a yields a promising result. Figure 4.14(a) shows the three measured isotherms on a relative vapor pressure axis revealing a shift of the top side of the evaporation rise to larger pressures going together with longer immersion times. At the same time, the bottom end of the condensation rise does not move to higher pressures. As it is closed pores that are dealt with (compare section 4.3.2), the top end of the evaporation branch corresponds to the pore diameter at the top and, whereas the bottom end of the condensation branch corresponds to the diameter at the (smaller) closed end. Therefore, the observed phenomenon implies an etch rate that weakens along the pore axis towards the closed end. For further analysis of this acid saturation, fig. 4.14(b) and fig. 4.14(c) show KELVIN diameter conversions of the relevant pressure ranges. For the pressure isotherms, the evaporation rises have an exponential shape. Therefore, the converted diameter offset increases linearly along the liquid fraction which corresponds to the position in along the pore axis of a funnelled pore. The etch rate gradient along the pore length as plotted in fig. 4.15(a) can be derived from the values noted in table 4.2. The corresponding shape evolution of a pore is illustrated in fig. 4.15(b).

At this point it is safe to say that the phosphoric acid saturates within the pores due to the lack



(a)



(b)

**Figure 4.13** SEM images with the aim to measure the thickness of the *barrier layer* of the membranes 296c' and 296e'.

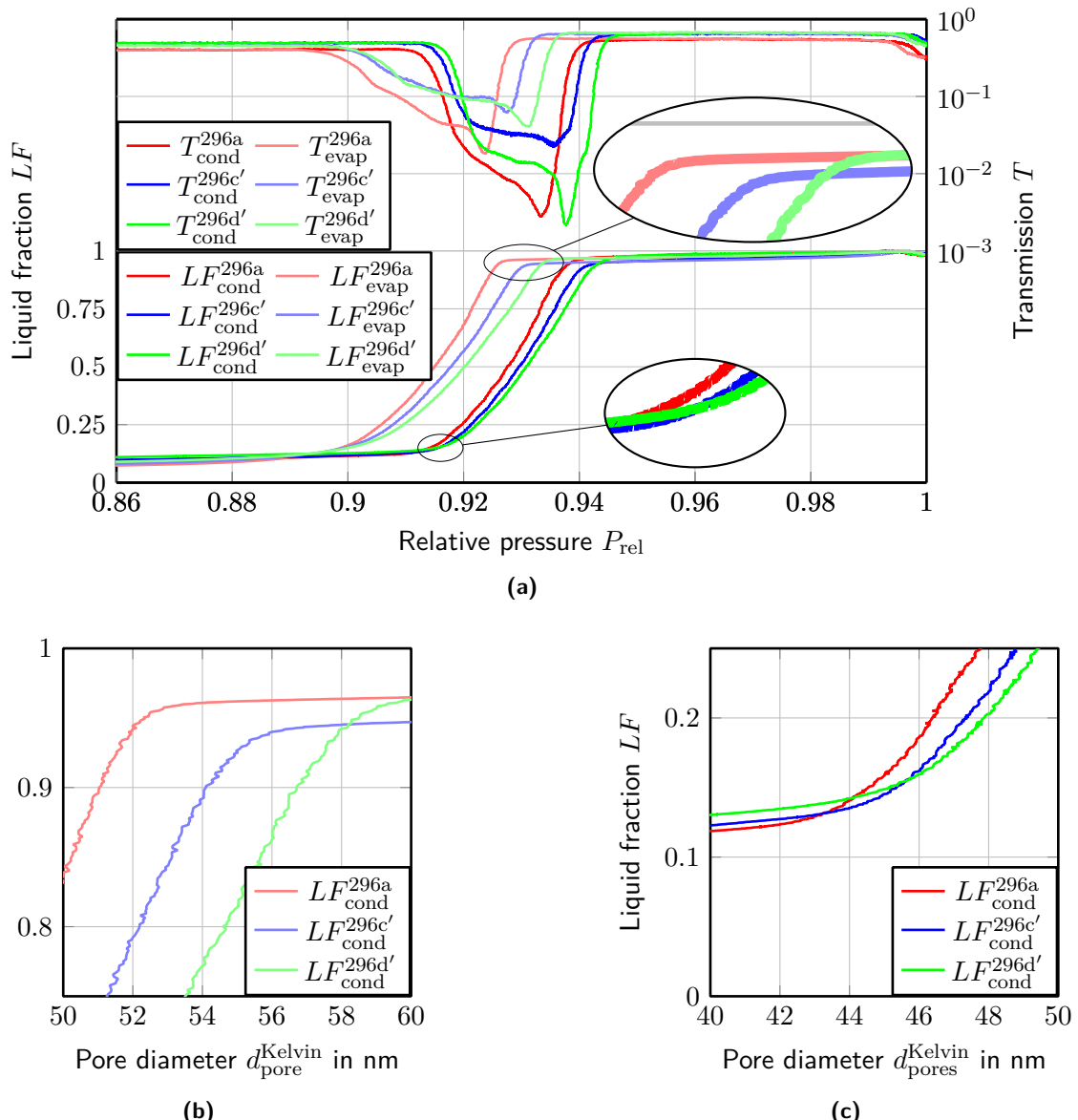


**Figure 4.14** Membrane 296c' has been immersed in phosphoric acid for  $t_{296c'} = 13 \text{ min}$ , 296d' for  $t_{296d'} = 26 \text{ min}$ . (a) shows the isotherms of the immersion experiment conducted using wafer 296. The shift to larger pressures of the beginning of the evaporation branch and the unmoving beginning of the condensation branch are clearly visible. (b) and (c) are higher resolution plots of the relevant areas of the evaporation and respectively condensation branch of the isotherm on a pore diameter scale.

**Table 4.2** Diameter reduction per minute of immersion derived from the isotherms of the membranes 296a, 296c, 296d.

$t_{\text{im}}[\text{min}]$	$\Delta d_{h=60 \mu\text{m}}[\text{nm}]$	$\Delta d_{h=0 \mu\text{m}}[\text{nm}]$
0	0	0
6,5	3	0
13	6	0

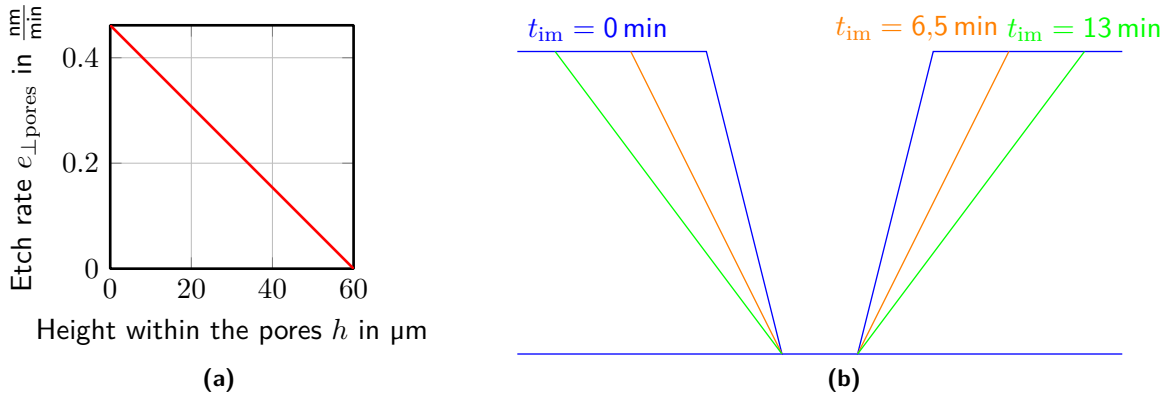


**Figure 4.15** Immersion of a closed pore membrane resulting in an increase of the funnelling aspect of the pores as shown in (b) due to the saturation of the acid within the pores. The visualized theory is backed by the isotherms in fig. 4.14(a) which lead to the etch rate dependency plotted in (a) on the height within a pore. For further explanations please refer to section 4.3.3.

of circulation.

#### 4.3.4 Inverse funnelling upon barrier layer dissolution

With the results of the immersion experiment explained above in section 4.3.4, the comparison of closed and open pore isotherms can be further analysed. Figure 4.16 shows two plots. Both compare the isotherm measured for a given membrane in closed state to the isotherm measured for the same membrane after the *barrier layer* dissolution. This permits the comparison disregarding the intra wafer dispersions that were concluded in section 4.2.4. The regarded membranes are 295b and 296b.

For both membranes, the trend of the isotherm to sharpen is clearly visible. Regarding the funnelling, the evaporation branch is of special interest. That it straightens upon the pore opening step implies that the funnelling decreases. Referring to the saturation of phosphoric acid within the pores upon immersion concluded in section 4.3.3, the inverse funnelling can be explained as follows: During the *barrier layer* dissolution the pores begin to open when the milky aspects appear. When they have disappeared, one might think the pores are open. But after having measure the bad open pores of wafer 294, Laurent Cagnon waits for another 15 min before removing the wafers from the acid. This is to be sure, that all pores are fully open without any constrictions on the aluminum side. In conclusion, the ophosphoric enters the pores from the small end saturates over at least 15 min. During that time, the pores are straightened (inverse funnelling) as the etch rate is larger on the small ends of the pores.

The attentive reader might have noticed the disappearance of the volumetric isotherm's kink of membrane 295b on the isotherm of open pore membrane 295b' that cannot be explained by the saturating acid. A possible interpretation of the occurrence of this case in the first place might be that the funnelling of the pores changes over abruptly at a certain uniform position

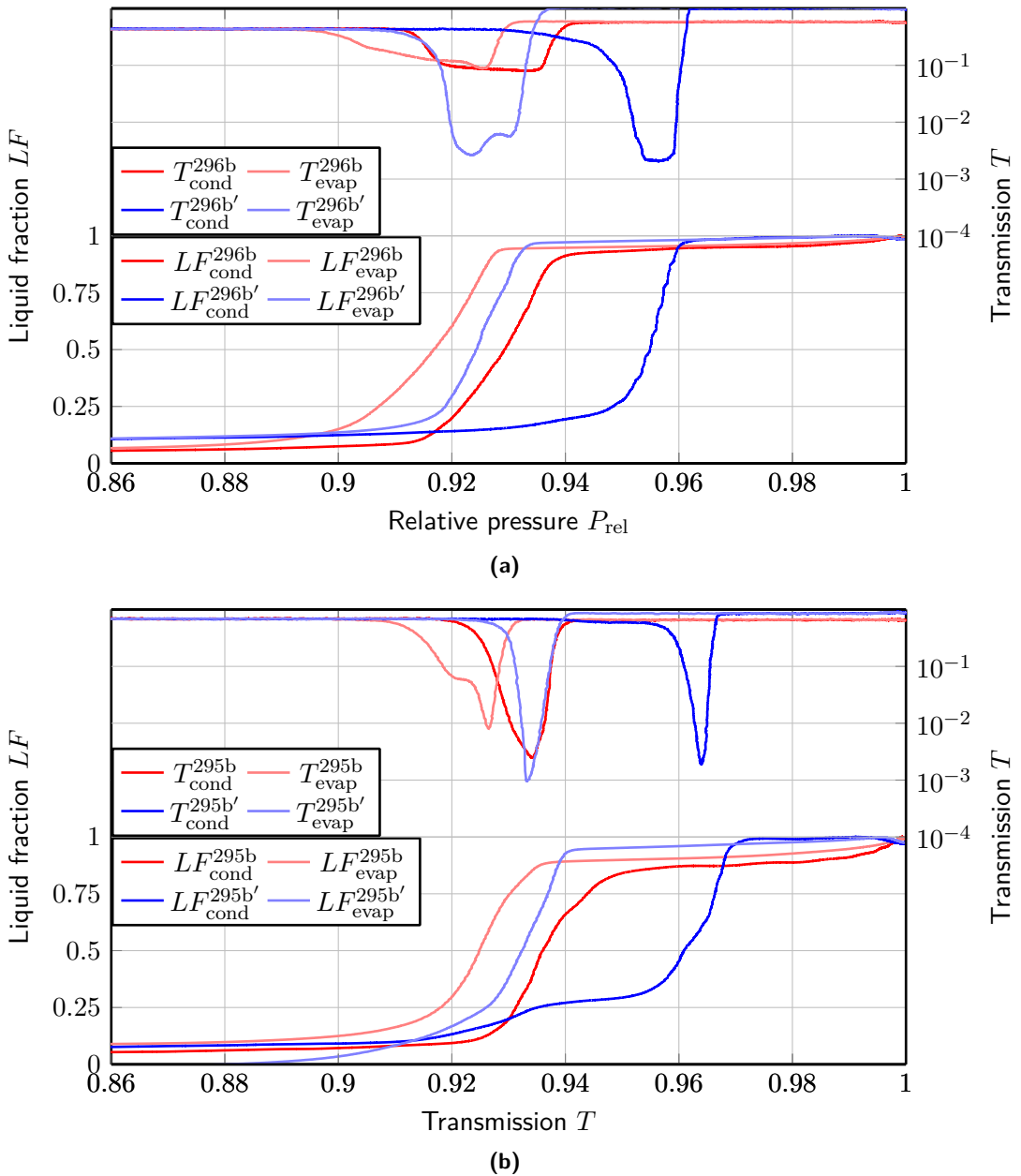


**Figure 4.16** Comparison of the isotherms of membranes with closed pores to those with open pores. (a) shows membranes of wafer 296, while (b) displays those of wafer 295. The increase of size of the hysteresis is clearly observable.

along the length of the pores (compare fig. 4.17). The correction of this phenomenon upon the *barrier layer* dissolution might be due to different etch rates of phosphoric acid on alumina that is contaminated by the chromatic acid used for the anodization of the wafers and pure alumina. To check this possibility, the thickness and formation of this layer must be taken into account and further experiments made. Due to the limited period of time of my internship, this theory has not yet been further explored.

However, a new defect appears on the comparison of membrane 295b and 295b': The open pore membrane 295b' shows a two step condensation branch, whereas the evaporation happens at a single pressure. What strikes the eye is that the first rise of the condensation branch spreads on the same relative pressure range as the evaporation branch. This raises the suspicion of pores filling at equilibrium pressure. Unlike the observations of bad open pore membrane 294op, the first rise of the condensation branch of membrane 295b' is followed by a plateau which leads to the next sharp rise. This implies two discreet pore populations of closed and open pores on the membrane, rather than bad open pores.

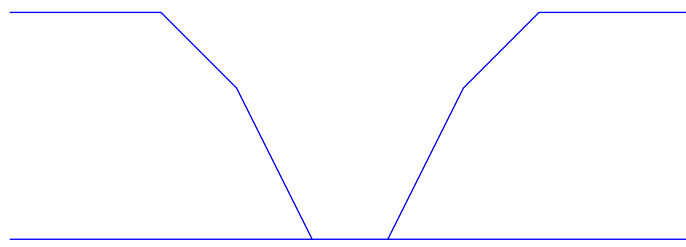


**Figure 4.17** Possible shape interpretation of the volumetric isotherms of membrane 295a for a single pore. If the interpretation were correct, an incontinuity ?? of the anodizing current could be the reason for the change in funnelling.

## Bibliography

[Cd15] Universität Konstanz: Corporate Design Manual. Universität Konstanz, (2015)